

# Strong-form meshless numerical modelling of visco-plastic material

Gašper Vuga<sup>a</sup>, Boštjan Mavrič<sup>b,a</sup>, Božidar Šarler<sup>a,b,\*</sup>

<sup>a</sup> Faculty of Mechanical Engineering, University of Ljubljana, Aškerčeva cesta 6, Ljubljana, SI-1000, Slovenia

<sup>b</sup> Institute of Metals and Technology, Lepi pot 11, Ljubljana, SI-1000, Slovenia

## ARTICLE INFO

### Keywords:

Strong-form meshless numerical modelling  
von Mises small strain visco-plasticity  
Polyharmonic splines  
Radial basis function generated finite differences

## ABSTRACT

This work extends our research on the strong-form meshless Radial Basis Function - Finite Difference (RBF-FD) method for solving non-linear visco-plastic mechanical problems. The polyharmonic splines with second-order polynomial augmentation are used for the shape functions. Their coefficients are determined by collocation. Three different approaches (*direct*, *composed*, and *hybrid*) are used for the numerical evaluation of the divergence operator in the equilibrium equation. They are presented and assessed for a visco-plastic material model with continuously differentiable material properties. It is shown that the *direct* approach is not suitable in this respect. In comparison to the previously investigated elasto-plasticity, it is shown that the *composed* approach can successfully cope with visco-plastic problems and is found to be even more accurate than the *hybrid* approach, which has previously proven to be most stable and effective in solving elasto-plasticity. This work extends the applicability of strong-form RBF-FD methods and opens up new areas of modelling non-linear solid mechanics.

## 1. Introduction

Physical phenomena describing shape changes of a solid body are generally governed by partial differential equations (PDEs). For some simple cases, those PDEs can be solved analytically. Still, very quickly, a sophisticated numerical method must be employed, where the domain of a solid body is spatially discretised, and the governing PDE is solved discretely in the form of a linear system of equations. Very well-known methods involving this process are the finite difference method (FDM) [1], finite element method (FEM) [2], finite volume method (FVM) [3], and boundary element method (BEM) [4]. The main drawback of the FDM is that the discretisation nodes must be aligned in the coordinate axis direction. All other methods rely on polygonisation or meshing of the domain, which can be a computationally complex and time-demanding process.

To eliminate the need for polygonisation, the meshless methods (MMs) emerged [5–10], where geometry is discretised by a cloud of nodes. This approach provides flexibility in handling complex geometries, moving boundary problems, and multidimensional challenges. Additionally, it allows for various types of discretisation adaptivity [11–13].

Many types of MMs have been developed to date. These can generally be divided into weak-form and strong-form MMs. Weak-form methods are stable, accurate and naturally satisfy Neumann boundary conditions (BCs). However, the need to create a background mesh, as with mesh-based methods, and the numerical integration makes

weak-form methods computationally intensive. In contrast, strong-form MMs use a direct discretisation of PDEs, for which no meshing is required [6].

In the field of solid mechanics, weak-form MMs have proven to be capable of tackling various non-linear problems, such as elasto-plasticity [14,15], elastodynamics [16], crack growth [17], and thermo-mechanical solidification analysis [18], to name a few.

In this paper, we investigate the possibility of modelling rate-dependent elasto-plasticity (also called visco-plasticity) with a strong-form MM. A special type, known as the Local Radial Basis Function Collocation Method (LRBFCM) [19–21], recently also Radial Basis Function generated Finite Difference (RBF-FD) method [22] is employed. It is based on a local approximation of the solution on the local support stencils. A combination of radial basis functions (RBFs) and monomials is used for the shape functions. A particular type of RBFs, the so-called polyharmonic splines (PHSs), are used since, in combination with monomials (augmentation), they guarantee the positive definiteness of the local interpolant. In addition, there is no free shape parameter, which generally occurs in typical RBFs [22]. In RBF-FD, the differential operators are discretised in a finite-difference sense; however, the nodes are not required to be aligned with the coordinate axis. The weight coefficients are computed separately for each local support stencil by inverting small, fully populated systems of equations.

\* Corresponding author at: Faculty of Mechanical Engineering, University of Ljubljana, Aškerčeva cesta 6, Ljubljana, SI-1000, Slovenia.

E-mail addresses: [gasper.vuga@fs.uni-lj.si](mailto:gasper.vuga@fs.uni-lj.si) (G. Vuga), [bostjan.mavric@fs.uni-lj.si](mailto:bostjan.mavric@fs.uni-lj.si) (B. Mavrič), [bozidar.sarler@fs.uni-lj.si](mailto:bozidar.sarler@fs.uni-lj.si) (B. Šarler).

The method has been successfully applied to various problems such as fluid flow during the continuous casting process [23–25], the influence of magnetic field on fluid flow [26,27], dendritic solidification [28–30], solid–solid phase transformations in aluminium alloys [31], micro combustion problems [32], financial option valuation [33], non-Newtonian fluid flow [34], compressible fluid flow [10], multi-scale modelling of hemodynamics [35], spread of an infectious disease [36], heating of steel billets in reheating furnace [37] to mention a few.

The RBF-FD has also been successfully used also on mechanical two-dimensional problems. Using Multiquadric RBFs, the following problems were investigated: linear elasticity problems [19,20,38], thermo-elasticity problems [39–41], mechanics of direct-chill casting of aluminium [42], and hot shape rolling process [43–46] with inclusion of casting defects [47]. Using PHSs, the RBF-FD was used on elastic problems [11] with the addition of sharp BCs [12], on the response of thoracic diaphragm [48], on elasto-plastic benchmark [49], and on thermo-mechanics of continuous casting of aluminium alloys [42] and steel [50]. Regarding non-linear mechanics, the works of [42,50] included computationally expensive numerical computation of the Jacobian, resulting in many non-linear iterations. In [49], the modified Newton-Raphson (NR) iteration algorithm was employed using only elastic material parameters for Jacobian composition. In [46], the direct iteration method was employed for solving a plastic material model.

In our previous work [51], we firstly presented RBF-FD approach for solving elasto-plasticity where NR algorithm was employed for iterative solving of non-linear equations. The constitutive equations were solved using the return mapping algorithm with the addition of a consistent tangent operator (CTO), which was used for the Jacobian (also stiffness matrix) update. Three RBF-FD discretisation approaches of balance equations, namely *direct*, *composed*, and *hybrid*, were presented where we found that only hybrid can solve elasto-plastic problem. We found that the direct approach is unsuitable for such problems since it diverges immediately. The direct approach performs well up to some point but suffers from an oscillatory solution that can eventually lead to divergence. For the hybrid approach, we found that it gives a bit less accurate results than the composed but overall performs much more stable with fewer Newton-Raphson iterations (NRIs) needed for convergence. The method has been extended in [52] for solving decoupled thermo-elasto-plasticity, and in [53] applied on thermo-mechanics of steel bars cooling on the cooling bed. The discretisation approaches differentiate how the divergence operator in the balance equation is discretised since it acts on stresses that are, due to material properties, non-smoothly differentiable on the interface of elastic to plastic transition.

In this work, we continue to study the previously introduced discretisation approaches to problems with non-linear, continuously differentiable material properties. The material model used is a rate-dependent (or visco-plastic) small-strain von Mises plastic model, where the strain rate is governed by the Norton-Hoff law. To achieve continuously differentiable material properties, the initial yield stress is set to zero. This means the material begins to flow under any non-zero stress, eliminating the transition from elastic to visco-plastic response.

Discretisation approaches are assessed on two benchmarks. We found that the *direct* approach is not suitable for solving such problems since it diverges. As opposed to the previous studies on elasto-plasticity [51], the *composed* approach performs similarly to the *hybrid* approach and gives a slightly more accurate results.

The main originality of the present work consists of the derivation, implementation, and verification of three RBF-FD discretisation approaches for solving non-linear elasto-viscoplasticity in two dimensions. This work represents the first strong-from meshless attempt at solving visco-plasticity with zero yield stress.

The present paper is structured in the following way; first, the governing equations of the mechanical model are given in Section 2. Numerical methods for discretisation and the solution procedure are presented in Section 3. In Section 4, the verification on two benchmarks is presented, and lastly, the conclusions are given in Section 5.

## 2. Physical model

The equilibrium of a continuum solid material occupying the domain  $\Omega$  is governed by the balance law

$$\nabla \cdot \boldsymbol{\sigma} + \mathbf{f} = 0 \quad \text{in } \Omega, \quad (1)$$

where  $\boldsymbol{\sigma}$  represents a Cauchy stress tensor and  $\mathbf{f}$  is the body force vector. A unique solution is obtained by applying the boundary conditions (BCs) on the boundary  $\Gamma = \Gamma_u \cup \Gamma_T \cup \Gamma_F$ . Three types of BCs are employed as

$$\begin{aligned} \mathbf{u} &= \bar{\mathbf{u}} && \text{on } \Gamma_u, \\ \boldsymbol{\sigma} \cdot \mathbf{n} &= \bar{\mathbf{t}} && \text{on } \Gamma_T, \\ \{u_n, t_t\} &= \{0, 0\} && \text{on } \Gamma_F, \end{aligned} \quad (2)$$

where displacement vector  $\bar{\mathbf{u}}$  is prescribed on  $\Gamma_u$ , traction vector  $\bar{\mathbf{t}}$  on  $\Gamma_T$ , and both components of displacement in normal direction  $u_n$ , and traction in tangential direction  $t_t$  are set to zero on  $\Gamma_F$ . The so-called free-slip BC applied on  $\Gamma_F$  restricts the material to move in the normal direction and allows the material to move freely in the tangential direction. Small strain tensor is defined as  $\boldsymbol{\varepsilon} = \nabla^s \mathbf{u}$  where  $\nabla^s = (\nabla + \nabla^T) / 2$  is the symmetric gradient operator.

The relationship between stress tensor and strain tensor is defined by Hooke's law

$$\boldsymbol{\sigma} = \mathbf{D}^e : \boldsymbol{\varepsilon}^e, \quad (3)$$

where  $\mathbf{D}^e$  represents the fourth-order elasticity tensor and is for isotropic material uniquely defined with a pair of independent constants such as Young's modulus  $E$  and Poisson ratio  $\nu$  or with a pair of so-called Lamé constants  $G$  and  $\lambda$ .

Within the small strain assumption, the total strain can be additively split into recoverable (elastic), and irrecoverable (inelastic or plastic) parts. Assuming a rate dependence of the material the additive split is defined in the rate form as

$$\dot{\boldsymbol{\varepsilon}} = \dot{\boldsymbol{\varepsilon}}^e + \dot{\boldsymbol{\varepsilon}}^{vp}, \quad (4)$$

where  $\boldsymbol{\varepsilon}^{vp}$  represents irrecoverable rate-dependent visco-plastic strain. Its evolution is defined by the flow rule

$$\dot{\boldsymbol{\varepsilon}}^{vp} = \dot{\gamma} \mathbf{N} = \dot{\gamma} \frac{\partial \Phi}{\partial \boldsymbol{\sigma}} = \dot{\gamma} \sqrt{\frac{3}{2}} \frac{\mathbf{s}}{\|\mathbf{s}\|}, \quad (5)$$

where  $\mathbf{N}$  is the Prandtl-Reuss flow vector that represents the flow direction and is defined as the derivative of the yield function  $\Phi$  over the stress tensor. Since zero yield stress is assumed, meaning that the material starts to flow at any non-zero deviatoric stress, the yield function is directly equal to the von Mises stress  $\Phi = \sigma_{vm}$ . This effective scalar quantity is defined as  $\sigma_{vm} = \sqrt{3J_2}$ , where  $J_2 = 1/2(\mathbf{s} : \mathbf{s})$  is the second invariant of the deviatoric stress tensor  $\mathbf{s} = \boldsymbol{\sigma} - \text{Itr}(\boldsymbol{\sigma})/3$ . The visco-plastic multiplier  $\dot{\gamma}$  that represents the magnitude of irreversible strain rate is an explicitly defined function of stress and is for here used Norton-Hoff (NH) law [54] defined as

$$\dot{\gamma}(\boldsymbol{\sigma}) = \left( \frac{\sigma_{vm}}{\mu} \right)^\beta, \quad (6)$$

where experimentally obtained parameters  $\mu$  and  $\beta$  are NH viscosity and NH exponent, respectively. Additionally, a visco-plastic multiplier is equal to the rate of the accumulated or effective visco-plastic strain

$$\dot{\gamma} = \dot{\boldsymbol{\varepsilon}}^{vp}, \quad (7)$$

where accumulated visco-plastic strain is defined as  $\boldsymbol{\varepsilon}^{vp} = \sqrt{\frac{2}{3}} \|\boldsymbol{\varepsilon}^{vp}\|$ . From the equations presented, it can be seen that the non-linearity is hidden in the definition of NH law (6). Since no condition on when the plastic flow occurs is present or any other additional condition, the material parameters are continuously differentiable.

The described model is usually used in modelling high-temperature processes such as metal casting [55–57] where temperatures are close to the melting temperature and the yield stress is effectively zero.

A more in-depth explanation of the described equations can be found in [2,58,59].

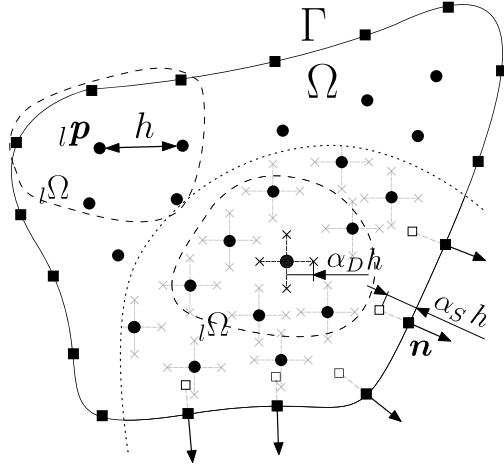


Fig. 1. Scheme of a generic domain  $\Omega$  with boundary  $\Gamma$ . The solid circles and squares represent interior and boundary nodes, respectively. The centre node of the subdomain  ${}_l\Omega$  is  ${}_l\mathbf{p}$  where the distance to the closest node is denoted with  $h$ .

### 3. Numerical method

#### 3.1. Spatial discretisation with RBF-FD

Within the RBF-FD approach, the observed domain is spatially discretised with homogeneous distribution of collocation nodes (CNs). The algorithm for scatter discretisation initially presented in [42] starts by positioning  $N_b$  nodes on the boundary  $\Gamma$ , then  $N_a$  inner nodes are generated where first the inner layer of nodes prescribed in the opposite direction of outward facing normal is generated. Then, the domain is filled with randomly positioned nodes that are, in the next step, homogeneously redistributed with a minimisation process. Regular node arrangements can also be employed, as in the FDM. Examples of node discretisation positioning are presented in Figs. 3(b) and 11(b) related to the studied cases that follow. One can see that the corner nodes are not included. This is due to a possible mismatch in the prescribed different boundary conditions meeting at the corner and an undefined normal vector at the corner [51].

To derive the method, we first observe a generic region  $\Omega$  with boundary  $\Gamma$  shown in Fig. 1, that is discretised with  $N$  CNs ( $N_b$  black squares and  $N_a$  black dots). For each point  ${}_l\mathbf{p}$  ( $l = 1, \dots, N$ ) the local support stencil  ${}_l\Omega$  is chosen by picking  ${}_lN - 1$  nearest neighbours where  ${}_lN$  is the number of nodes within  ${}_l\Omega$  including the centre point  ${}_l\mathbf{p}$ .  $h$  denotes the distance to the nearest neighbour.

Within each local support stencil  ${}_l\Omega$  a local solution function  ${}_ly_\xi(\mathbf{p})$ , where  $\xi = 1, \dots, n_d$  runs over space dimensions  $n_d$ , is approximated as a weighted sum

$${}_ly_\xi(\mathbf{p}) \approx \sum_{i=1}^{{}_lN} \alpha_{i,\xi} {}_l\Phi_i(\mathbf{p}) + \sum_{i=1}^M \alpha_{({}_lN+i),\xi} p_i(\mathbf{p}) = \sum_{i=1}^{{}_lN+M} \alpha_{i,\xi} {}_l\Psi_i(\mathbf{p}). \quad (8)$$

Basis functions are compactly written as  $\Psi_i(\mathbf{p})$  that are either RBFs  ${}_l\Phi_i(\mathbf{p})$  ( $i \leq {}_lN$ ) or monomials  $p_i(\mathbf{p})$  ( $i > {}_lN$ ). Interpolation coefficients are denoted with  $\alpha_{i,\xi}$ , ( $i = 1, \dots, {}_lN + M$ ).

In this work, polyharmonic splines (PHSs) are used as RBFs [22]. The PHS defined on  ${}_l\Omega$  and centred at the  ${}_l\mathbf{p}_i$ , where  $i = 1, \dots, {}_lN$ , is in the dimensionless form written as

$${}_l\Phi_i(\mathbf{p}) = \left( \frac{\|\mathbf{p} - {}_l\mathbf{p}_i\|}{h} \right)^m, \quad (9)$$

where  $m$  represents the order of PHS that is here equal to  $m = 3$ , and  ${}_lh$  is the average distance from the central node defined as

$${}_lh = \sqrt{\sum_{i=2}^{{}_lN} \frac{\|\mathbf{p} - {}_l\mathbf{p}_i\|^2}{{}_lN - 1}}. \quad (10)$$

PHSs, compared to other RBFs, do not include any free shape parameter that can be difficult to select. As shown in [22], when using augmented PHSs, the  $h$ -converge is governed by the augmentation order if the condition on the minimum number of nodes in a local support domain is satisfied  ${}_lN \gtrsim 2M$ , where  $M = \binom{p+n_d}{p}$ .

Going back to local interpolation (8) it can be written as a system of  $n_d({}_lN + M)$  equations

$$\sum_{\chi=1}^{n_d} \sum_{i=1}^{{}_lN+M} {}_lA_{ji,\xi\chi} \alpha_{i,\chi} = {}_lY_{j,\xi}, \quad (11)$$

where  ${}_lA_{ji,\xi\chi}$  is the interpolation matrix defined as

$${}_lA_{ji,\xi\chi} = \begin{cases} \Psi_i({}_l\mathbf{p}_j) \delta_{\xi\chi} & \text{if } {}_l\mathbf{p}_j \in \Omega \\ p_{j-{}_lN}({}_l\mathbf{p}_i) \delta_{\xi\chi} & \text{if } j > {}_lN \text{ and } i \leq {}_lN, \\ 0 & \text{otherwise} \end{cases}, \quad (12)$$

and  ${}_lY_{j,\xi}$  is the vector of known values defined as

$${}_lY_{j,\xi} = \begin{cases} y_\xi({}_l\mathbf{p}_j) & \text{if } {}_l\mathbf{p}_j \in \Omega \\ 0 & \text{otherwise.} \end{cases} \quad (13)$$

Next, we introduce a general differential operator  $\mathcal{L}$  that preserves the rank of the physical field. The acting of the  $\mathcal{L}$  on the local interpolation function (8) is written as

$$\mathcal{L}{}_ly(\mathbf{p})_\xi = \sum_{\chi=1}^{n_d} \mathcal{L}_{\xi\chi} {}_ly_\chi(\mathbf{p}) \approx \sum_{\chi=1}^{n_d} \sum_{i=1}^{{}_lN+M} \alpha_{i,\chi} \mathcal{L}_{\xi\chi} {}_l\Psi_i(\mathbf{p}), \quad (14)$$

where it can be seen that  $\mathcal{L}$  is acting only on the basis functions. Interpolation coefficients can be expressed from Eq. (11) as

$${}_l\alpha_{i,\chi} = \sum_{\zeta=1}^{n_d} \sum_{j=1}^{{}_lN+M} {}_lA_{ij,\chi\zeta}^{-1} {}_lY_{j,\zeta}, \quad (15)$$

Inserting this definition in Eq. (14), we arrive at

$$\begin{aligned} \mathcal{L}{}_ly(\mathbf{p})_\xi &\approx \sum_{\zeta=1}^{n_d} \sum_{j=1}^{{}_lN+M} {}_lY_{j,\zeta} \sum_{\chi=1}^{n_d} \sum_{i=1}^{{}_lN+M} {}_lA_{ij,\chi\zeta}^{-1} \mathcal{L}_{\xi\chi} {}_l\Psi_i(\mathbf{p}) \\ &\approx \sum_{\zeta=1}^{n_d} \sum_{j=1}^{{}_lN+M} {}_lY_{j,\zeta} {}_l\mathcal{W}_{j,\xi\zeta}(\mathbf{p}), \end{aligned} \quad (16)$$

where the right side of the expression is compactly denoted as  ${}_l\mathcal{W}_{j,\xi\zeta}(\mathbf{p})$  that represents operator coefficients. From here, it can be seen that the operator acting on the interpolant is expressed as a weighted sum of known values and operator coefficients, similar to the FDM, where operator coefficients are known in advance. Here, operator coefficients are computed in the preprocessing step for each local support, and each differential operator type needed. After operator coefficients are determined, the discretisation of the governing PDEs and BCs can be performed where the global sparse system is generated in the next step.

#### 3.2. Incremental approach for solving non-linear visco-plastic problem

The presented visco-plastic mechanical model is non-linear. The solution depends on the loading history and the loading rate. To solve such a model, a general time-dependent external load is applied incrementally in consecutive time steps  $t_n$ ,  $n \in \{1, n_{max}\}$ , where the time differential is defined as  $\Delta t = t_{n+1} - t_n$ . For simplicity, only index  $n$  is used in the following. At  $(n + 1)$ th load (or  $t_{n+1}$  time) increment the balance Eq. (1) can be written as

$$\mathbf{f}^{int}|_{n+1} - \mathbf{f}^{ex}|_{n+1} = \mathbf{r}(\mathbf{u}_{n+1}), \quad (17)$$

where  $\mathbf{f}^{ex}$  represents the external force, and  $\mathbf{r}$  is the residual that should converge to zero. The internal force is defined as  $\mathbf{f}^{int} = \nabla \cdot \boldsymbol{\sigma}$ . Since the constitutive model is non-linear, the residual is linearised as

$$\nabla \cdot (\mathbf{D}\nabla^s) \Big|_{n+1}^{i-1} \delta \mathbf{u} = -\mathbf{r}|_{n+1}^{i-1}, \quad (18)$$

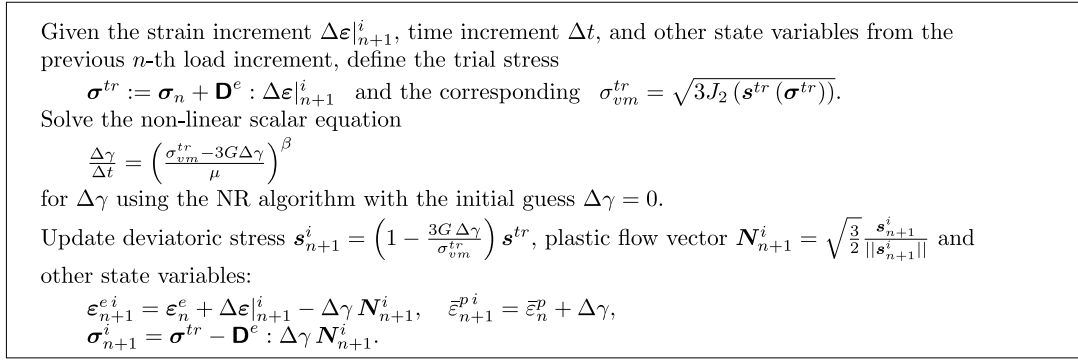


Fig. 2. Time integration algorithm for the von Mises visco-plasticity with Norton-Hoff law without an initial yield stress.

and solved iteratively for  $\delta \mathbf{u}$  via the Newton–Raphson iteration algorithm, where  $i$  represents the iteration index. The Jacobian is compactly written as  $\mathbf{K}_T = \nabla \cdot (\mathbf{D}\nabla^s)$ , where  $\mathbf{D} = \partial \boldsymbol{\sigma} / \partial \boldsymbol{\varepsilon}$  is the tangent operator that is numerically computed consistently to the local time integration scheme employed for solving constitutive equations (4)–(7) (see Section 3.3). With the solution for  $\delta \mathbf{u}$ , the displacement increment is updated as  $\Delta \mathbf{u}^i = \Delta \mathbf{u}^{i-1} + \delta \mathbf{u}$ . From here on, the strain increment is computed by definition as  $\Delta \boldsymbol{\varepsilon}^i = \nabla^s (\Delta \mathbf{u}^i)$  that represents the input value for the local iteration explained in Section 3.3. From there, stresses, other state variables, and the tangent operator are computed. With a new stress solution, the internal force is computed again, and by Eq. (18), a new residual value. If convergence tolerance  $\|\mathbf{r}\|_{n+1}^i / \|\mathbf{f}^{ext}\|_{n+1} \leq e_{tol}^{NR}$ , is satisfied the displacement is updated as  $\mathbf{u}_{n+1} = \mathbf{u}_n + \Delta \mathbf{u}^i$  and a new loading step is applied ( $n = n + 1$ ), else the  $\mathbf{K}_T$  is updated with the new  $\mathbf{D}$  and a new iteration is performed ( $i = i + 1$ ). The  $e_{tol}^{NR}$  represents the convergence tolerance.

The incremental procedure is applied similarly to the BCs included in the global system of equations.

### 3.3. Time integration of visco-plastic material model

At first, given the strain increment, the stress trial solution is predicted as purely elastic. Then, a set of constitutive equations (4)–(7) is solved by the return mapping algorithm, where Implicit Euler time stepping is employed. It can be shown that using the von Mises equivalent stress in connection with the Prandtl-Reuss flow vector, solving non-linear constitutive equations is reduced to solving a single non-linear scalar equation in  $\Delta \gamma$  [2]. The only non-linearity comes from the NH exponent  $\beta$ . If  $\beta = 1$ , then  $\Delta \gamma$  is explicitly determined. The procedure is summarised in Fig. 2.

With the solution for  $\Delta \gamma$ , the consistent tangent operator can be defined in the following form

$$\mathbf{D}_{n+1}^i = \mathbf{D}^e - \frac{6G^2 \Delta \gamma}{\sigma_{vm}^{tr}} \mathbf{I}_d + 6G^2 \left( \frac{\Delta \gamma}{\sigma_{vm}^{tr}} - \frac{1}{3G + \frac{\mu}{\beta \Delta t} \left( \frac{\Delta \gamma}{\Delta t} \right)^{\beta-1}} \right) \tilde{\mathbf{N}}_{n+1}^i \otimes \tilde{\mathbf{N}}_{n+1}^i \quad (19)$$

where  $\mathbf{I}_d$  represents the deviatoric projection tensor and  $\tilde{\mathbf{N}} = \mathbf{N} / \|\mathbf{N}\|$  the unit flow vector.

### 3.4. Discretisation approaches with RBF-FD

Spatial discretisation of Eq. (18) can be performed in different ways. In this work three different approaches based on the RBF-FD method are presented. The discretisation of BCs is performed the same way in all approaches. For stabilisation of BCs, evaluation points of operator coefficients are shifted in the opposite direction of the boundary normals, as shown in Fig. 1 on the lower-right boundary. The distance between the boundary node and the evaluation point is defined as  $\alpha_s h$ .

#### 3.4.1. Direct approach

The direct approach was employed in all previous studies on linear and non-linear mechanics [11,46,49,50,60]. It is based on the analytical evaluation of the divergence operator in Eq. (18), which results in

$$[(\nabla \cdot \mathbf{D}) : \nabla^s + \mathbf{D} : \nabla \otimes \nabla^s] \delta \mathbf{u} = -\mathbf{r}, \quad (20)$$

where for clearance, indices  $i$  and  $n$  are omitted. Differential operators  $\nabla \cdot$ ,  $\nabla^s$  and  $\nabla \otimes \nabla^s$  are locally discretised via RBF-FD in each node and then, according to relation (20), expanded into the global stiffness matrix  $\mathbf{K}_T$ . The internal force is computed as the divergence on the solution stress field as  $\mathbf{f}^{int} = \nabla \cdot \boldsymbol{\sigma}$ . It can be seen that this definition is in terms of numerical discretisation inconsistent with the left term in (20), which is also calculated by taking the divergence of the stress tensor.

#### 3.4.2. Composed approach

To obtain the consistent discretisation between the Jacobian and the internal force, this approach starts the discretisation of the stress field as

$$\delta \boldsymbol{\sigma} = (\mathbf{D}\nabla^s) \delta \mathbf{u}, \quad (21)$$

where the term  $(\mathbf{D}\nabla^s)$  is expanded into a global rectangle sparse matrix denoted here as  $\mathbf{K}_\sigma$ . Next, the divergence operator is numerically discretised via RBF-FD and expanded into another global rectangle sparse matrix denoted as  $\mathbf{K}_{div}$ . To obtain the final global stiffness matrix, these two are simply multiplied as  $\mathbf{K}_T = \mathbf{K}_{div} \mathbf{K}_\sigma$ . Compared to the *direct* approach, only two 1<sup>st</sup>-order operators are discretised here. Internal force is computed as in the previous approach, where discretisation is now consistent with the Jacobian.

#### 3.4.3. Hybrid approach

In the *hybrid* approach, the idea is to numerically discretise the divergence operator via FDM. Observing Fig. 1 below the dotted line, it can be seen that to each inner CN, there is a virtual 2nd-order FD stencil assigned presented with four additional virtual nodes (crosses). Using the local support that belongs to the central node, the coefficients of the term  $(\mathbf{D}\nabla^s)$  are computed first via RBF-FD as in the *composed* approach. However, the coefficients are not evaluated in the central node but in all the virtual nodes that belong to the central node. Then, the divergence operator is discretised using the computed coefficients as in the FDM. The obtained coefficients are then (as in the *direct* approach) expanded to the global stiffness matrix  $\mathbf{K}_T$ . The internal force is also computed via FDM, where stress values computed on virtual nodes are used. The distance between a CN and corresponding virtual nodes is defined as the product of the FD stencil size parameter  $\alpha_D$  and the smallest inter-nodal spacing  $h$ . Compared with previous approaches, the local iteration is performed four times more due to the virtual nodes. A similar approach was first introduced in [61], where variables were interpolated using RBF-FD on the 2nd-order FD stencils prescribed to each CN, and all operators were discretised with the FDM.

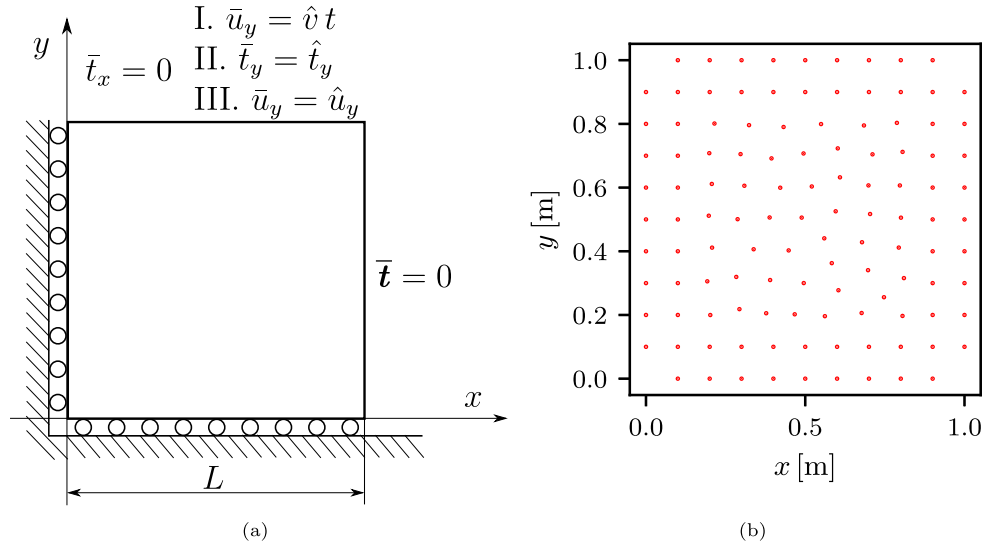


Fig. 3. (a) scheme of the uniaxial case test with the geometry and boundary conditions. (b) geometry discretisation with node spacing  $h = 0.025$  m.

#### 3.4.4. Numerical implementation

The represented approaches are coded in Fortran 2018 programming language and compiled with Intel Fortran Compilers 2021.1.1. The computations were performed on a personal computer with an Intel(R) Core(TM) i7-8750H CPU, with six cores and a maximum clock speed of 4.10 GHz.

### 4. Numerical examples

The presented approaches are tested on two different benchmarks. In the first benchmark, the solution is constant over the field and only time-dependent. In the second benchmark, the solution is time and spatially dependent. Both benchmarks are defined in a plane strain approximation.

#### 4.1. Uniaxial case test

Proposed discretisation approaches are first applied on a uniaxial benchmark, shown in Fig. 3(a). A square with the side length  $L$  is on the right side free to move in all directions (zero traction vector). On the left and the bottom side, free slip BC is employed. On the top side, the material is free to move in the tangential direction, and in the normal direction, three different loading regimes are employed to investigate different visco-plastic phenomena. First (I.), a linearly increasing displacement in time (constant strain rate) is employed to check the *strain rate dependence*. Second (II.), a constant traction is applied to check the *creep* response, and lastly (III.), a constant displacement is applied to check for the *relaxation* response. No accumulated strains or stresses are present in the material at time zero.

The obtained solutions are effectively zero-dimensional since all tensorial values are constant over the field. From here, it follows that the problem can be reduced to a system of first-order non-linear ordinary differential equations (ODEs). An example ODEs derivation process is for the loading regime I. presented in Appendix A. The reference solution (RS) is obtained with the Wolfram Mathematica software [62], where the system of ODEs is numerically solved employing the eighth-order Runge–Kutta solver with the fixed time step  $10^{-4}$  s.

Material parameters used with geometry dimension are listed in Table 1. The geometry discretisation with scattered node arrangement used in RBF-FD approach studies is shown in Fig. 3(b), where the node spacing is set to  $h = 0.025$  m.

The numerical parameters are listed in Table 2. For the 2<sup>nd</sup>-order augmentation, as suggested in [22],  ${}_lN$  should be at minimum  ${}_lN = 12$ ,

Table 1

Uniaxial test case parameters.

Computational domain	Unit	Value
Size of the domain ( $L$ )	m	1
Material parameters		
Young's modulus ( $E$ )	Pa	1
Poisson's ratio ( $\nu$ )	/	0.3
NH exponent ( $\beta$ )	/	1.1
NH viscosity ( $\mu$ )	Pa s	1.1

Table 2

Numerical parameters used in an uniaxial test case.

Numerical parameters	
PHS power ( $m$ )	3
Augmentation order ( $\rho$ )	2
Number of nodes in the support domain ( ${}_lN$ )	13
FD stencil size parameter ( $\alpha_D$ )	0.5
Boundary stabilisation parameter ( $\alpha_S$ )	0
N-R convergence tolerance ( $\epsilon_{tol}^{NRR}$ )	$10^{-6}$
Max number of N-R iterations ( $NRI_{max}$ )	50

to achieve the 2<sup>nd</sup>-order  $h$ -convergence. Here, we choose  ${}_lN = 13$ . Concerning the *hybrid* approach, it was previously shown [51] in the linear-elastic cases that taking  $\alpha_D$  close to 1 reduces the  $h$ -convergence order and stability but, on the other hand, improves the accuracy at fixed  $h$ . Taking  $\alpha_D$  close to 0.1 preserves the augmentation-governed  $h$ -convergence order. Therefore, the parameter is chosen approximately in between, i.e.  $\alpha_D = 0.5$ . Since the solution is constant in space, it was found that no need for the BCs stabilisation is needed, so  $\alpha_S = 0$ . Time frame observed is  $\{t_{start}, t_{end}, \Delta t\} = \{0, 10, 10^{-2}\}$  s where time step  $\Delta t$  is 100 times larger than the one used for the RS.

#### 4.1.1. Time dependent results

Figs. 4–6 show the comparison between RSs and solutions obtained with the *hybrid* approach for all three loading regimes. Only *hybrid* approach solutions are demonstrated since it was found that the other two approaches give the same solution, which is shown in Appendix B, and can also be seen from the error in Fig. 7. Strain components  $\epsilon_{xx}(t)$ ,  $\epsilon_{yy}(t)$  ( $\epsilon_{zz}$  is here omitted) and stress components  $\sigma_{yy}(t)$ ,  $\sigma_{zz}(t)$  ( $\sigma_{xx}(t) = 0$ ) are shown over time. Two different hat values (see BCs in Fig. 3(a)) are used to show the loading size dependence.

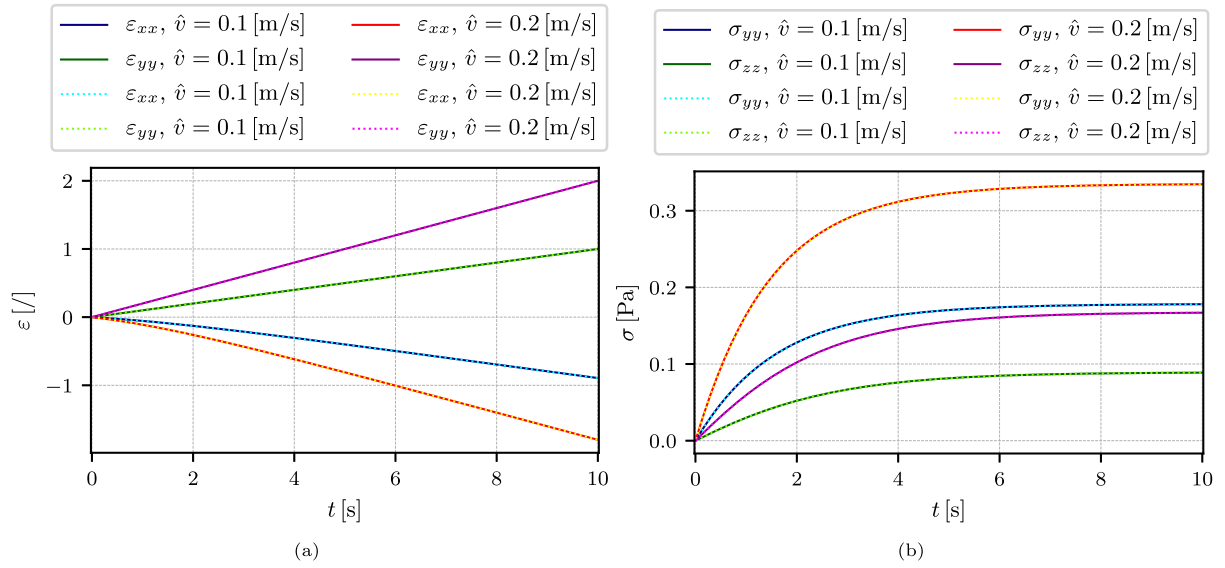


Fig. 4. I. strain rate dependence. Evolution of (a) strains and (b) stresses with time for two different loading velocities.

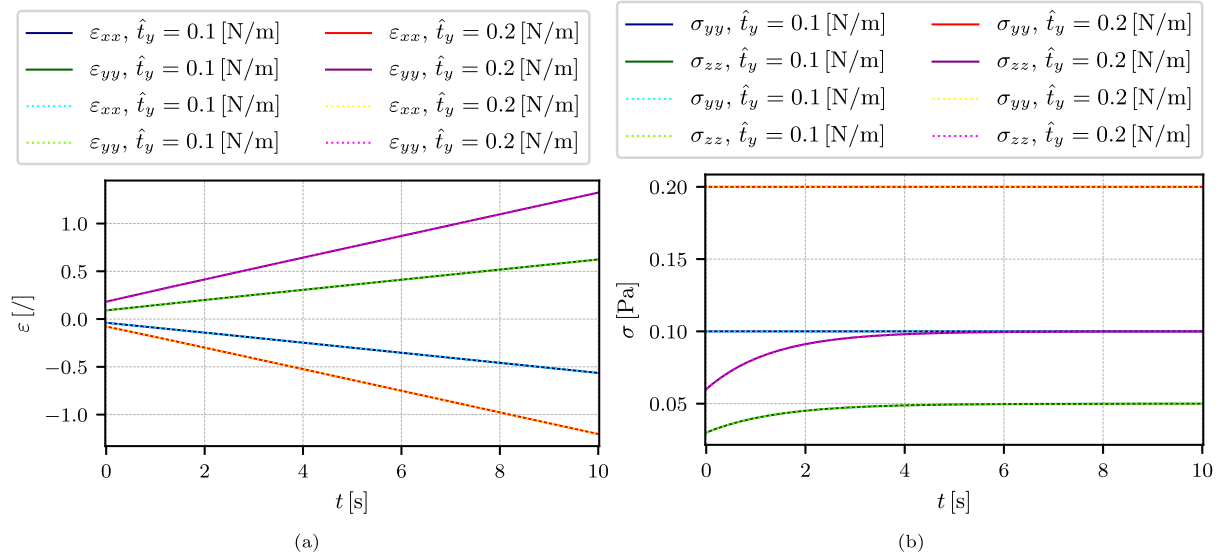


Fig. 5. II. creep response. Evolution of (a) strains and (b) stresses with time for two different traction loadings.

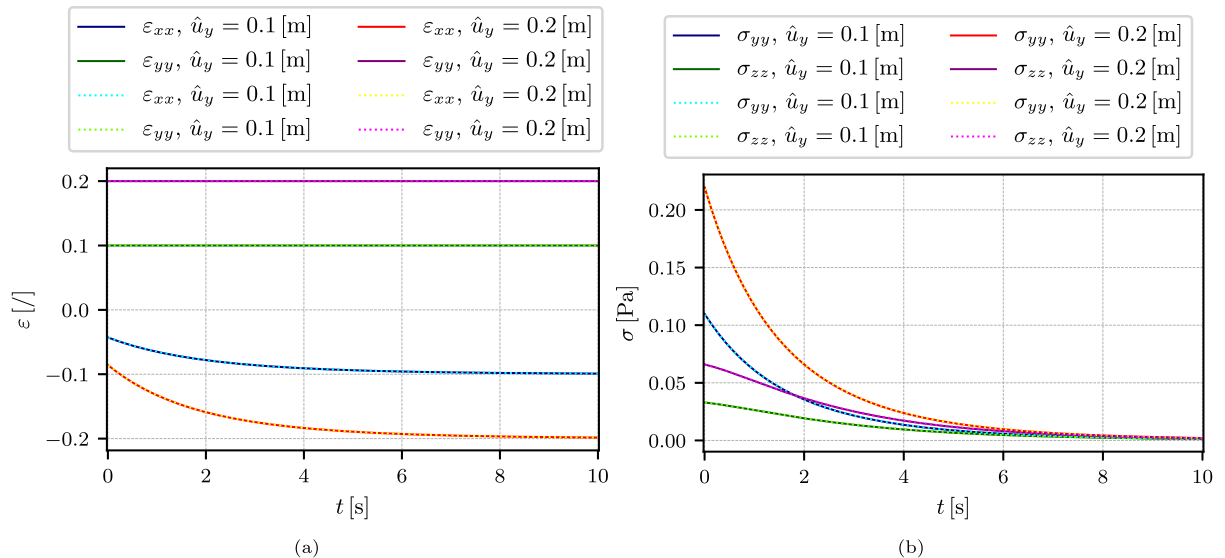


Fig. 6. III. relaxation response. Evolution of (a) strains and (b) stresses with time for two different displacement loadings.

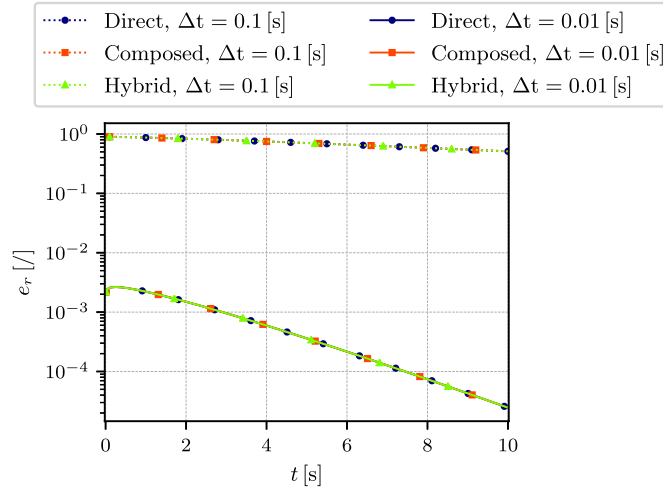


Fig. 7. Relative error  $e_r$  in  $\sigma_{yy}$  as a function of time for all approaches using two different time steps.

In Fig. 4(a) it can be seen that applying larger strain rates induces larger strains. Similarly, it can be seen in Fig. 4(b) where with larger strain rates, stresses reach larger limit values. The rate at which the limit values are reached is the same since the NH visco-plastic parameters are kept the same.

In Fig. 5(a), an instant (elastic) strain larger at a larger traction load can be observed at time zero. Due to the creep effect, the strains are then increasing, and in the case of larger traction, they are at a higher rate. In terms of stresses, the  $\sigma_{yy}$  is constant and equal to the prescribed load. The elastic part of  $\sigma_{zz}$  is observed instantly and then increases until it reaches the limit value, from where the stresses are constant.

In Fig. 6(a),  $\varepsilon_{yy}$  is constant and equal to the prescribed load.  $\varepsilon_{xx}$  is gradually decreasing and, in limit, reaches the final value. Due to the relaxation, the initial elastic stresses fall until the material reaches a zero stress state, as seen in Fig. 6(b).

To investigate the accuracy, we look at the relative error over time in  $\sigma_{yy}$  defined as

$$e_r(t) = \frac{|\sigma_{yy}(t) - \sigma_{yy}^{RS}(t)|}{|\sigma_{yy}^{RS}(t)|}, \quad (22)$$

where  $\sigma_{yy}$  is obtained with RBF-FD approaches and  $\sigma_{yy}^{RS}$  is the RS. Results are shown in Fig. 7 for the I. strain rate response at fixed  $\dot{v} = 0.2$  m/s example. Two different time steps are used where one is 100 $\times$  and the other 1000 $\times$  larger than the one used in the RS. Results obtained with all of the proposed approaches are shown. It can be seen that  $e_2$  is reducing with time step and that is falling in time meaning the stresses are reaching the actual limit stress value. No difference between approaches can be seen.

#### 4.1.2. Non-linear iteration convergence

Next, the convergence in terms of the NR algorithm is investigated again on the strain rate response case I. Fig. 8 shows the residual for the first 75 accumulated Newton–Raphson iterations (NRIs) is shown where black empty markers represent the residual at a first NRI ( $i = 1$ ) at some load increment  $n$ . It can be seen that to reach the convergence tolerance  $e^{NR}$ , three iterations are needed. Also, in terms of the NR convergence, no difference between approaches can be seen.

#### 4.1.3. Properties of stiffness matrices

As shown, all of the introduced approaches are successful at solving this benchmark. Next, the structure of resulting global stiffness matrices (SMs) generated with proposed approaches is investigated. In Fig. 9, sparse SMs generated on  $N = 117$  that include BCs, are shown. Non-zero values are presented with black dots. It can be seen that SMs obtained with the *direct* and *hybrid* approaches possess the same

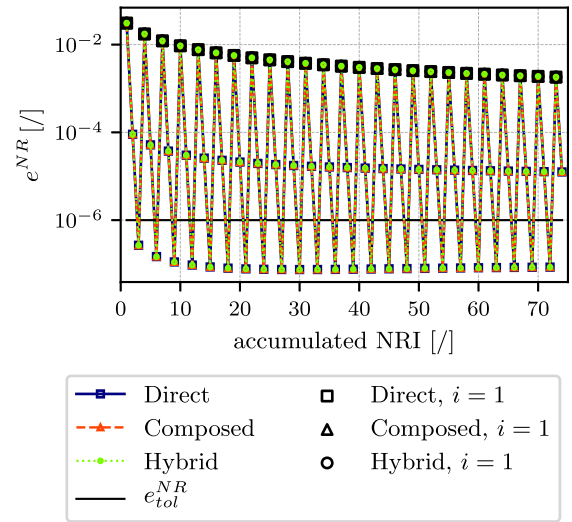


Fig. 8. NR residual  $e^{NR}$  for the first 75 accumulated NRIs for all proposed approaches.

Table 3

Condition numbers of the stiffness matrices using different discretisation approaches.

Approach	$\kappa$ [ ]
<i>direct</i>	$66.35 \cdot 10^3$
<i>composed</i>	$7.758 \cdot 10^3$
<i>hybrid</i>	$39.38 \cdot 10^3$

structure. SM generated with the *composed* approach has a similar structure but includes more non-zero elements. From the computational memory perspective, *direct* and *hybrid* approaches are more desirable since they require less space.

The number of non-zero elements (NNZE) in the system grows with the number of CNs ( $N$ ), as shown in Fig. 10. It can be seen that the increasing rate is similar, but the amount is for the *composed* approach approximately three times larger.

Next we compute the condition number of the SM  $\kappa = \sigma_{max}(\mathbf{K}_T)/\sigma_{min}(\mathbf{K}_T)$ , where  $\sigma_{max}$  and  $\sigma_{min}$  are maximum and minimum singular values [63]. In Table 3 the results for all approaches are shown. It can be seen that the *composed* approach is least sensitive to the numerical noise and that *direct* approach is the most sensitive.

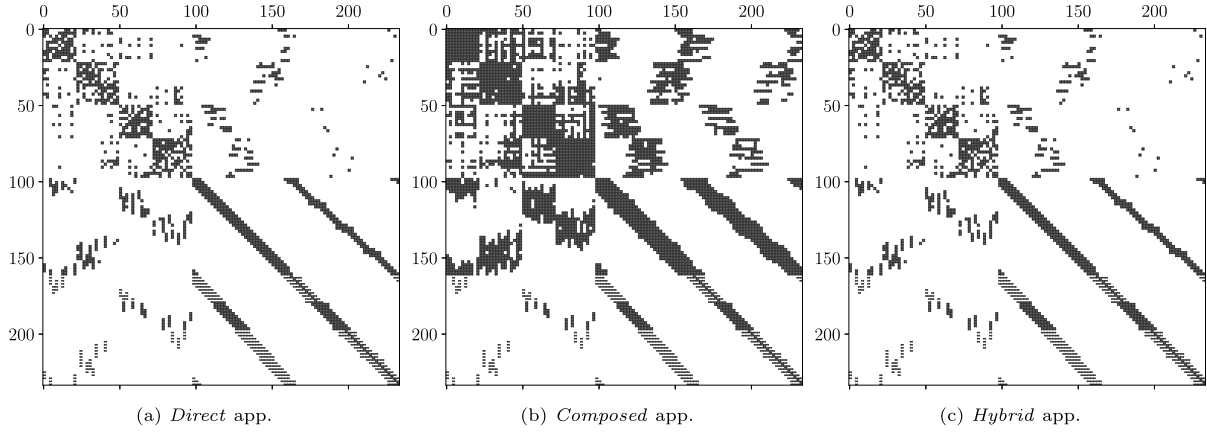


Fig. 9. Stiffness matrix examples for (a) *direct*, (b) *composed*, and (c) *hybrid* approach including BCs on  $N = 117$ .

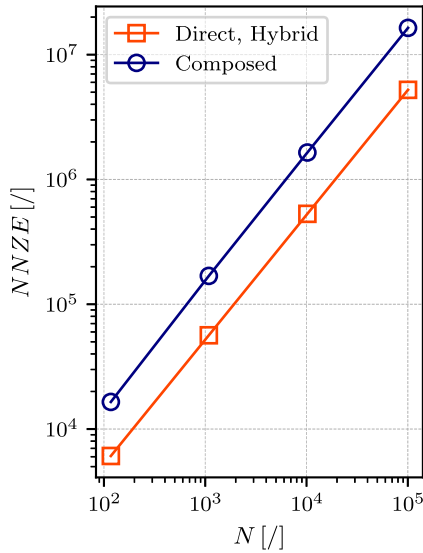


Fig. 10. Number of non-zero elements (NNZE) in stiffness matrix as a function of a number of CNs ( $N$ ).

#### 4.2. Plate with a hole problem

The following case considers a plate with a hole initially presented in [42]. The geometry with BCs is shown in Fig. 11(a). The plate is compressed by applying a constant velocity load on the top side. No accumulated strains or stresses are present in the material at time zero. An example of scattered node positioning with  $h = 0.025$  m is shown in Fig. 11(b). Since the solution is space-dependent, different behaviour of the proposed discretisation approaches are expected to be observed.

Material parameters, geometry, and loading size are listed in Table 4. The chosen NH parameters are computationally much more challenging than the one used in the previous case. They are taken such that they represent the actual metal response at high temperatures [64]. The time frame observed is  $\{t_{start}, t_{end}, \Delta t\} = \{0.5 \cdot 10^{-3}, 10^{-5}\}$  s. The numerical parameters used are the same as in the previous case (Table 2) except for  $\alpha_D$  and  $\alpha_S$ . The size of  $\alpha_S$  is elaborated upon in the subsequent section.

Regarding the *hybrid* approach and  $\alpha_D$ , it was previously shown in [51] that in a case of elasto-plasticity  $\alpha_D$  should not be too small ( $\alpha_D < 0.3$ ) otherwise, the elasto-plastic front cannot be captured,

Table 4

Plate with a hole benchmark parameters.

Computational domain	Unit	Value
Size of the domain ( $L$ )	m	1
Radius of the hole ( $a$ )	m	0.25
Material parameters		
Young's modulus ( $E$ )	MPa	70
Poisson's ratio ( $\nu$ )	/	0.3
NH exponent ( $\beta$ )	/	5
NH viscosity ( $\mu$ )	MPa s	0.1256
Load		
Prescribed velocity ( $\dot{v}$ )	m/s	-0.1

and the solution diverges. In this study, no elasto-visco-plastic front is present (no initial yield stress), and the tangent operator, which includes material properties is continuously differentiable. It was also shown that with increasing  $\alpha_D$  the accumulative number of NRI is also increasing. Concerning these findings and the previously mentioned preservation of  $h$ -convergence at small values, the parameter is picked as  $\alpha_D = 0.1$ .

In [42] the Norton-Hoff law is defined a bit differently as  $\dot{\gamma} = A_0 \left( \frac{\sigma_{em}}{\sigma_0} \right)^{n_0}$ , where parameters are set to  $A_0 = 10^{-2} \text{ s}^{-1}$ ,  $\sigma_0 = 5 \text{ kPa}$ , and  $n_0 = 5$ . With NH definition (6), the parameters are computed as  $\mu = A_0^{-1/n_0} \sigma_0$  and  $\beta = n_0$ .

The reference solution (RS) was obtained with the finite element method (FEM) where the program package [65] was employed. The unstructured meshing of the domain was performed with 19890 4-noded quadrilateral elements where mesh density was kept constant. The approximate size of the element was set such that a similar amount of unknowns were used in FEM and RBF-FD approaches.

To use the same visco-plastic material model within [65], a user specified *Flow stress* and *Creep* functions are defined. *Power law* flow stress is defined as  $\bar{\sigma} = c \bar{\epsilon}^m + \gamma$ , where all parameters are set to zero except for the *initial yield stress*  $\gamma = \sigma_0$ . *Power law* creep function has a general form of  $\dot{\epsilon} = \gamma (\sigma/S)^m$ , where parameters are set as  $\gamma = A_0$ ,  $m = n_0$ , and  $S$  is equal to the flow stress.

##### 4.2.1. Approaches performance without BCs stabilisation

First, the impact of the BCs stabilisation is explored, for which it was shown that it is not needed in a case of a constant solution field. In Fig. 12(a) the residual for the first 75 accumulated NRIs is shown for the case with no BC stabilisation ( $\alpha_S = 0$ ). It can be seen that the *direct* approach immediately diverges, where for  $i > 5$  residual

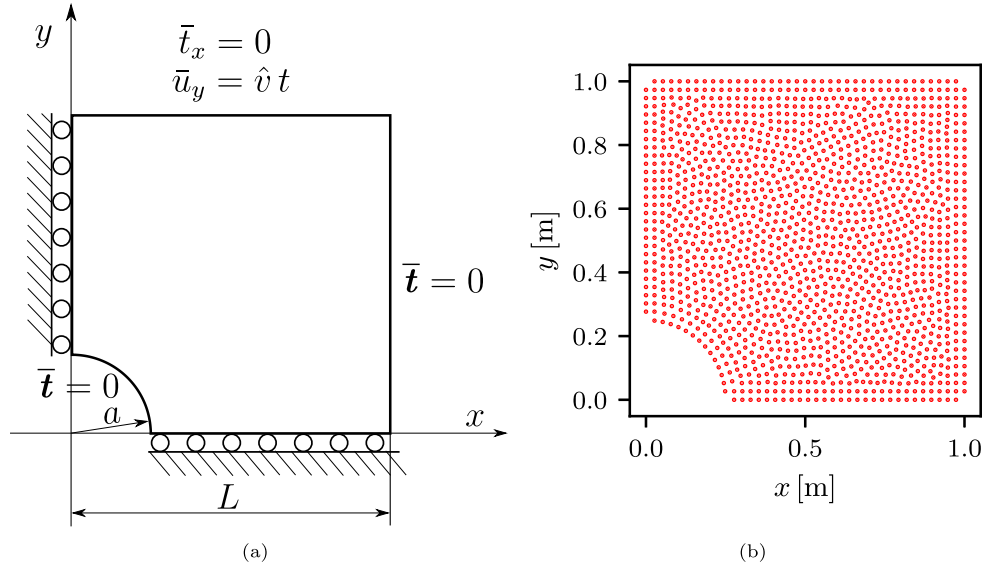


Fig. 11. (a) Scheme of the plate with a hole problem with geometry and boundary conditions. (b) Geometry discretisation with  $h = 0.025$  m.

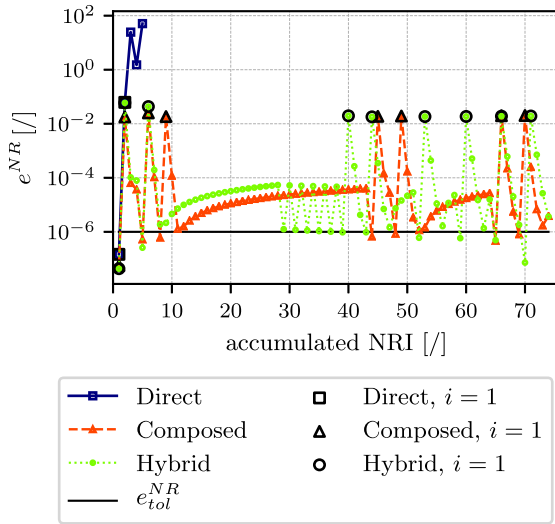


Fig. 12. NR residual  $e^{NR}$  for the first 75 accumulated NRIs for all proposed approaches obtained without BC stabilisation ( $\alpha_S = 0$ ).

is not plotted since it grows further. In the other two approaches, the converged residual increases with each load step and diverges at some point.

An example of  $\sigma_{xx}(p)$  solution fields obtained with *composed* and *hybrid* approaches at  $n = 1$  are shown in Fig. 13 for the case of no BCs stabilisation. It can be seen that in a region of stress concentrations towards the boundary, the solution is oscillatory.

In Fig. 14 the residual obtained using BCs stabilisation ( $\alpha_S = 0.5$ ) is shown. The *direct* approach again diverges, but the other two approaches converge successfully.

From the results, it can be concluded that, as in the case of elastoplasticity [51], also here with visco-plasticity, the *direct* approach is not suitable for tackling space-dependent problems. The reason for that is the inconsistent discretisation of the Jacobian and the internal force. The discretisations are consistent in the other two approaches, and approaches converge successfully.

Regarding the size of  $\alpha_S$ , it was previously shown in [51] that increasing  $\alpha_S$  decreases the accuracy, but as shown here, the use of it is inevitable for the approaches to converge. Picking  $\alpha_S$  too small can have little or no effect on the stabilisation, especially on coarse discretisations. On the other hand, taking it close to 1 the solution is spoiled. To be on the safe side  $\alpha_S = 0.5$  is used.

The next section presents results obtained with *composed* and *hybrid* approaches using BC stabilisation. Since BCs are stabilised, no oscillations are induced on the boundary.

#### 4.2.2. Analysis of solution fields at different times

Here, solutions of displacement component  $u_x(x, y = 0.5 \text{ m}, t = 16 \cdot 10^{-4} \text{ s})$  and stress component  $\sigma_{zz}(x, y = 0.5 \text{ m}, t = 16 \cdot 10^{-4} \text{ s})$  are presented over the line at a fixed time step. Different discretisation densities are applied with node spacings of  $h_i = 0.1/2^{i-1} \text{ m}$ ,  $i \in \{1, \dots, 5\}$ .

In Fig. 15 displacement over line is shown for both approaches. For clarity, an absolute error  $e_{abs} = |u_x^{FEM}(x) - u_x(h_i, x)|$  is added, and results obtained on  $h_1$  are not presented.

It can be seen that in both approaches, solutions converge to the FEM solution. From error plots, one can see that the *composed* approach produces much more accurate results.

In Fig. 16, stress  $\sigma_{zz}$  over line is shown for both approaches. The absolute error is defined in the same way as for the displacements. Again, it can be seen that the solution converges with decreasing node spacing and that the *composed* approach is more accurate. The error is more oscillatory than the displacement results, and as seen for the *hybrid* approach, it increases towards the boundary. The reason for that lies in the shifted positions where BCs are evaluated.

In Figs. 17 and 18, solutions of accumulated visco-plastic strain  $\bar{\epsilon}^{vp}(p, t = 16 \cdot 10^{-4} \text{ s})$  and von Mises stress  $\sigma_{vm}(p, t = 16 \cdot 10^{-4} \text{ s})$  are presented over field, respectively. Results are obtained on  $h_5$  node spacing which gives a similar number of variables to the RS.

It can be seen that both approaches produce very similar results and are very close to the FEM solutions. Since corner nodes are in here presented approaches omitted, problems are not exactly the same, so small differences compared to FEM are expected.

Additionally, accumulated visco-plastic strain  $\bar{\epsilon}^{vp}(p, t = t_{end})$  and von Mises stress  $\sigma_{vm}(p, t = t_{end})$  at the end of the simulation is presented in Figs. 19, and 20, respectively.

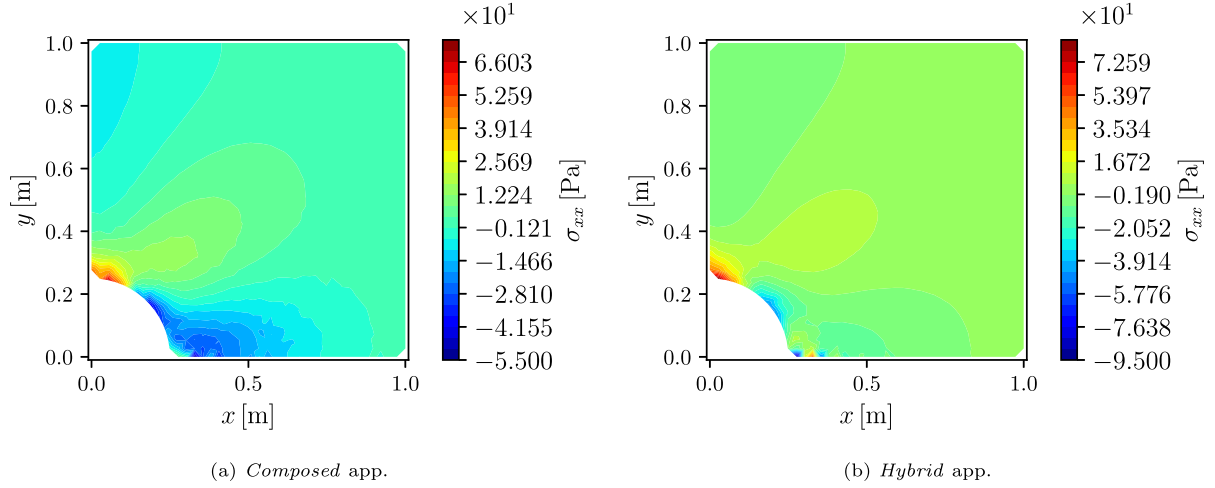


Fig. 13. First time step solution of  $\sigma_{xx}(p)$  obtained without BCs stabilisation ( $\alpha_S = 0$ ) using  $h = 0.025$  m; (a) *composed* approach, (b) *hybrid* approach.

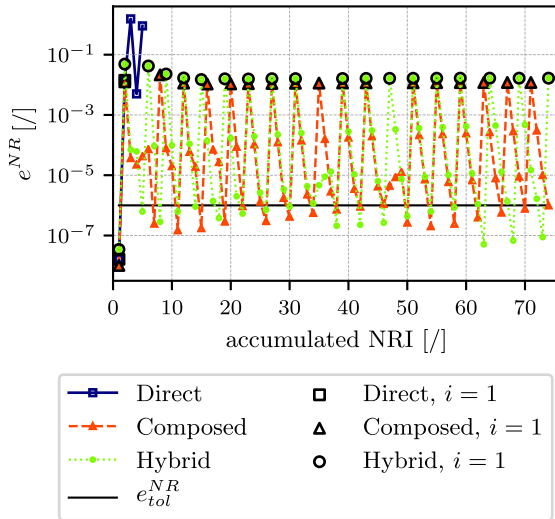


Fig. 14. NR residual  $e^{NR}$  for the first 75 accumulated NRIs for all proposed approaches obtained with BC stabilisation ( $\alpha_S = 0.5$ ).

One can see that the results are in good agreement with the FEM solutions. Regarding  $\sigma_{vm}$  (Fig. 20), it is evident that the solution from the *composite* approach is more closely aligned with FEM compared to the solution from the *hybrid* approach.

#### 4.2.3. Convergence analysis of approaches

To test the convergence of approaches, a relative  $L_2$  norm  $e_2$  is employed as

$$e_2 = \sqrt{\frac{\sum_{i=1}^N (y_i - \hat{y}_i)^2}{\sum_{i=1}^N \hat{y}_i^2}}, \quad (23)$$

where  $y$  is a solution variable investigated, and  $\hat{y}$  is a reference solution (RS). Index  $i$  runs over all nodes in the domain  $N$ . Solutions used for convergence study are taken at time  $t = 16 \cdot 10^{-4}$  s.

The presented model is temporarily discretised with the implicit Euler scheme, where the employed time step affects the accuracy of the solution. In Fig. 21 the convergence of the relative error  $e_2$  is shown where the RS is obtained at  $\Delta t = 5 \cdot 10^{-6}$  s. Geometry discretisation was performed using node spacing  $h_3$ .

First-order convergence is expected using an implicit Euler scheme. It can be seen that both approaches converge at a similar rate that is a bit higher than first order. Stress values converge at a bit higher rate and are compared to displacements more accurate.

With the decreasing time step, the residual or difference between the applied and inner forces becomes smaller. From here, it naturally follows that fewer Newton–Raphson iterations (NRIs) are needed for the residual to reach the convergence tolerance. In Fig. 22, the average number of NRIs used within one load increment is shown as a function of the time step employed. It can be seen that increasing the time step for one decade almost doubles the number of NRIs needed. Small differences between approaches can be observed.

In Fig. 23, the  $h$ -convergence is presented where the RS was obtained on node spacing  $h_5/2$ . Comparing approaches it can be seen that the stresses converge at a similar order ( $\sim 1.5$ ). Displacements in the *hybrid* approach converge with a similar order as stresses, but in the *composed* approach, they converge with a higher order ( $\sim 2$ ). The *composed* approach has a somewhat more typical trend where stresses have a lower order of convergence and are less accurate compared to displacements. Besides the BCs stabilisation, for which it was shown in [51], that it can reduce the order of convergence up to one order when using  $\alpha_S > 0.2$ , the augmentation-ordered convergence is still preserved in the *composed* approach. In the *hybrid* approach, the effect of BCs stabilisation is more evident but still does not spoil the convergence for the whole order. Overall, the *composed* approach is more accurate, and it can be seen that displacements are for a decade more accurate.

## 5. Conclusions

This work presents a first attempt at using a strong-form meshless method for solving visco-plastic material response with continuously differentiable material parameters.

Three different RBF-FD-based discretisation approaches (*direct*, *composed*, and *hybrid*) are implemented that differ in evaluating the divergence operator in the balance equation. Approaches are tested on two different benchmarks.

All approaches produced the same solution in the first benchmark, which possesses only time dependency. All of the visco-plastic phenomena were successfully verified. For such a case, it was shown that boundary condition stabilisation was not needed. For the *composed* approach, it has been shown that the stiffness matrix has approximately three times more non-zero values that can affect the computational memory and number of operations in iterative matrix inversion.

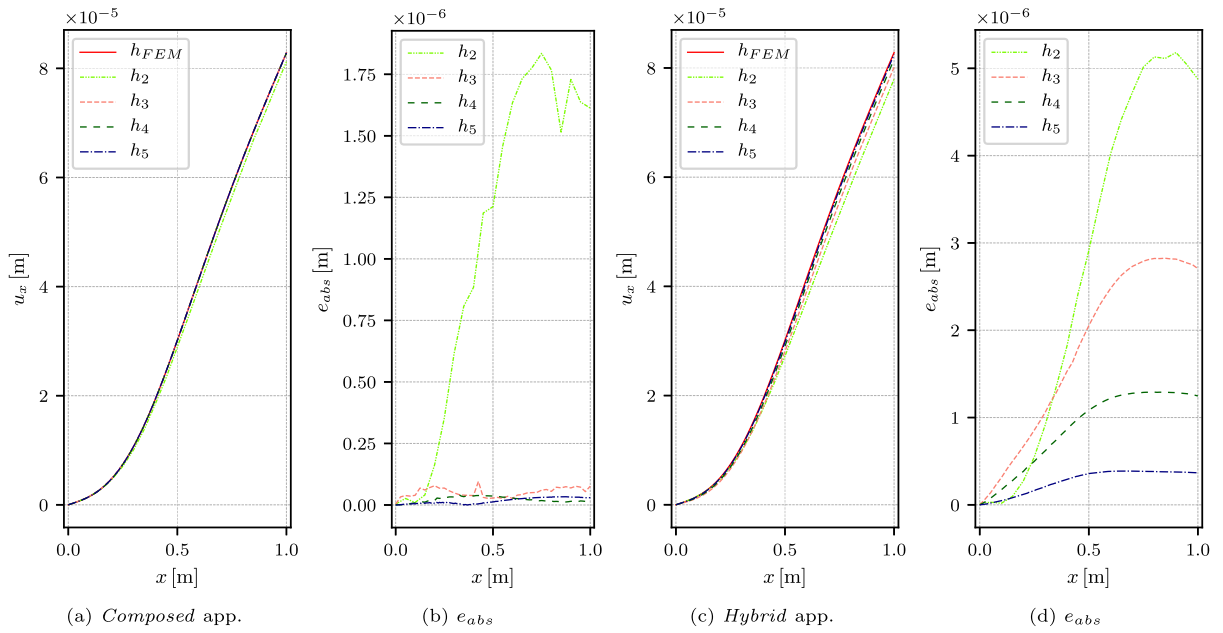


Fig. 15. Composed approach; (a)  $u_x(x, y = 0.5 \text{ m}, t = 16 \cdot 10^{-4} \text{ s})$ , (b) corresponding absolute error. Hybrid approach; (c)  $u_x(x, y = 0.5 \text{ m}, t = 16 \cdot 10^{-4} \text{ s})$ , (d) corresponding absolute error.

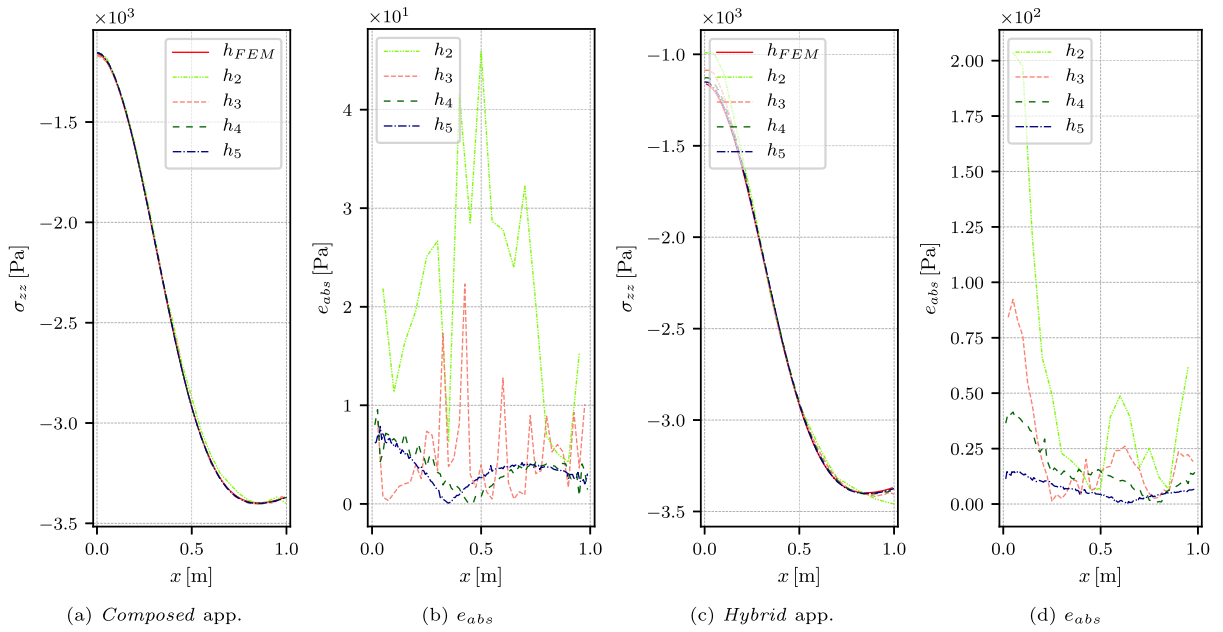


Fig. 16. Composed approach; (a)  $\sigma_{zz}(x, y = 0.5 \text{ m}, t = 16 \cdot 10^{-4} \text{ s})$ , (b) corresponding absolute error. Hybrid approach; (c)  $\sigma_{zz}(x, y = 0.5 \text{ m}, t = 16 \cdot 10^{-4} \text{ s})$ , (d) corresponding absolute error.

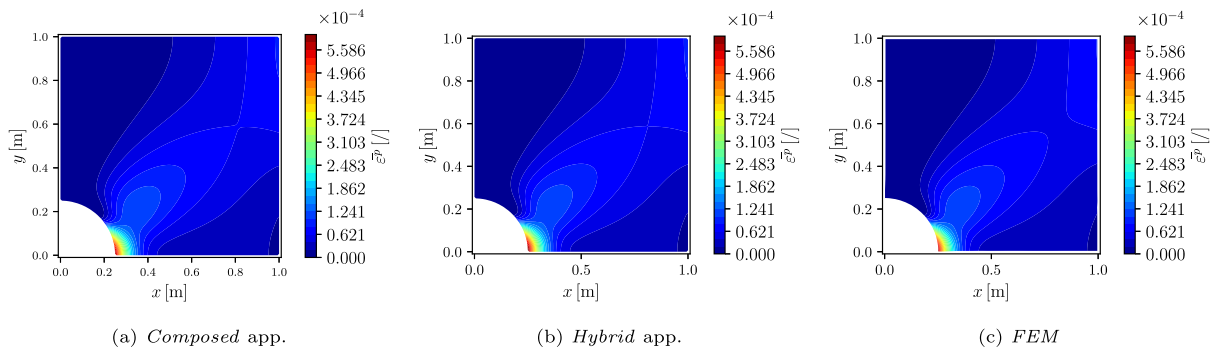


Fig. 17. Accumulated visco-plastic strain  $\bar{\epsilon}^{vp}(p, t = 16 \cdot 10^{-4} \text{ s})$ ; (a) composed approach, (b) hybrid approach, (c) FEM.

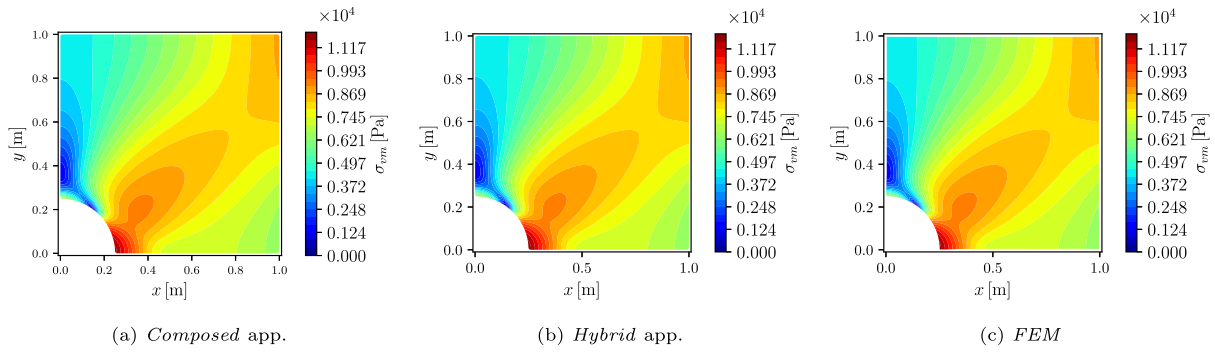


Fig. 18. Von Mises stress  $\sigma_{vm}(\mathbf{p}, t = 16 \cdot 10^{-4} \text{ s})$ ; (a) *composed* approach, (b) *hybrid* approach, (c) FEM.

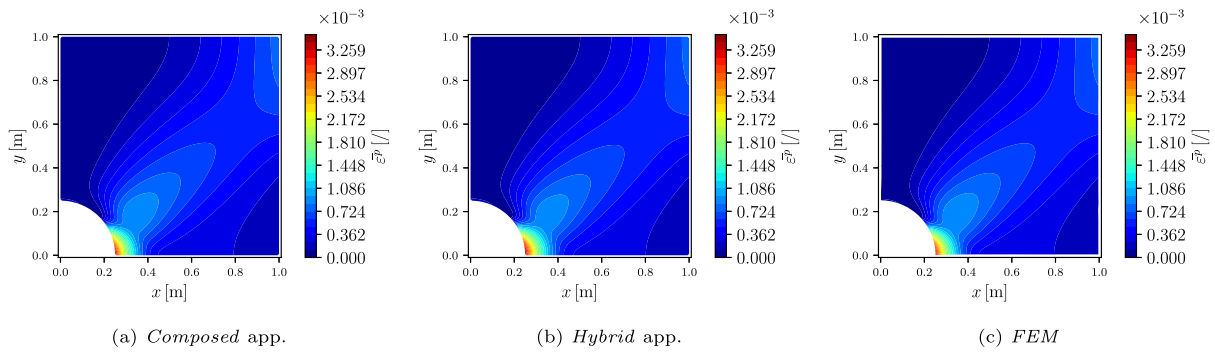


Fig. 19. Accumulated visco-plastic strain  $\bar{\epsilon}^{vp}(\mathbf{p}, t = t_{end})$ ; (a) *composed* approach, (b) *hybrid* approach, (c) FEM.

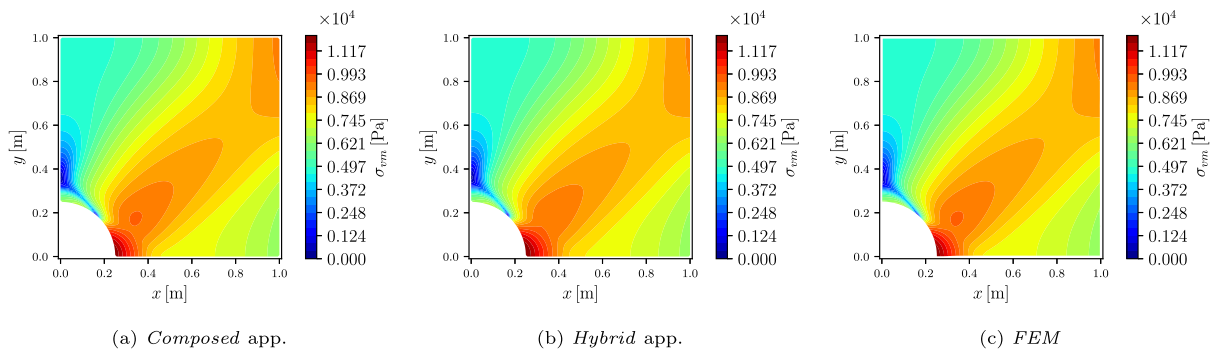


Fig. 20. Von Mises stress  $\sigma_{vm}(\mathbf{p}, t = 16 \cdot 10^{-4} \text{ s})$ ; (a) *composed* approach, (b) *hybrid* approach, (c) FEM.

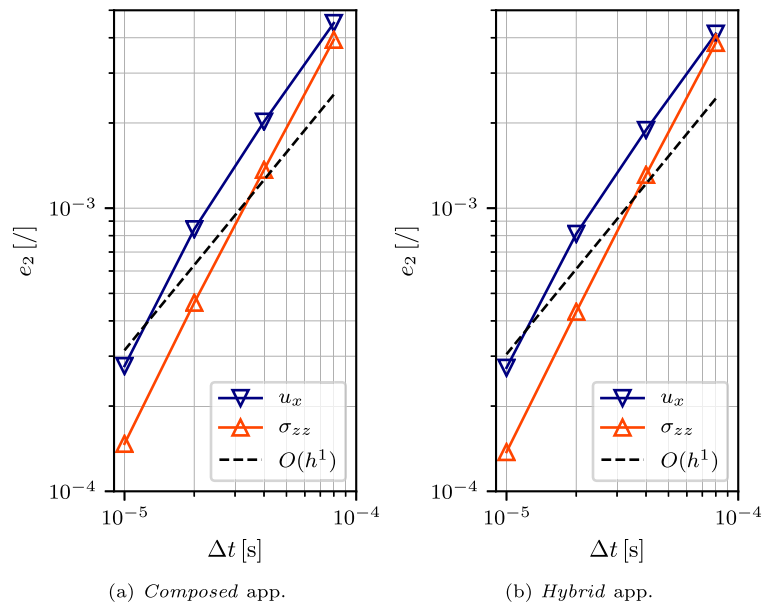


Fig. 21. Time step  $\Delta t$  convergence; (a) *composed* approach, (b) *hybrid* approach.

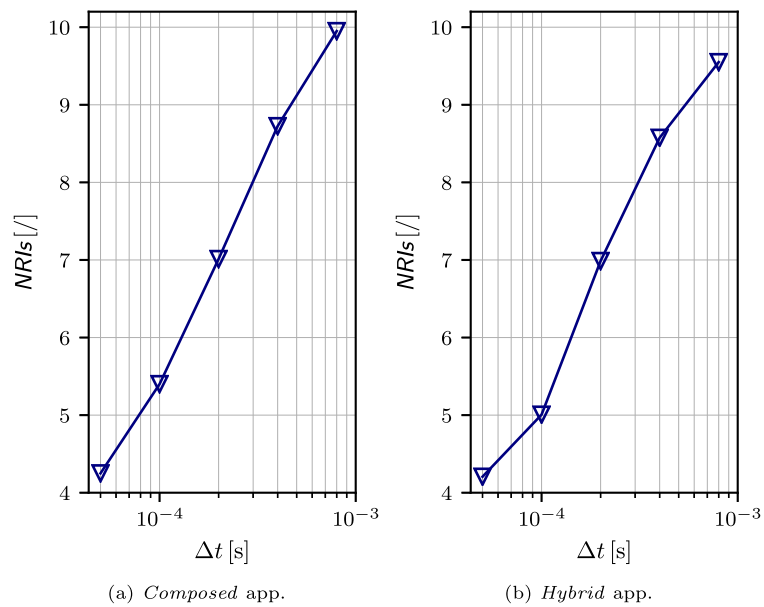


Fig. 22. Average number of Newton-Raphson iterations (NRIs) as a function of a time step; (a) *composed* approach, (b) *hybrid* approach.

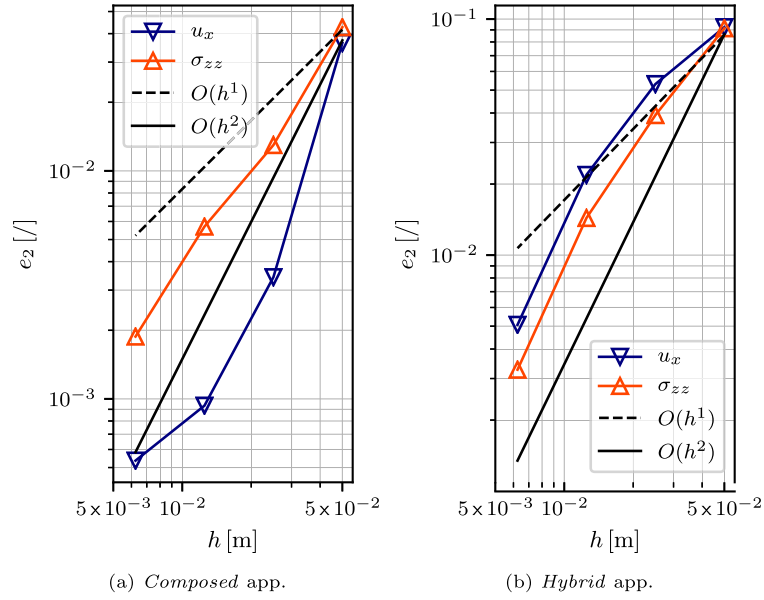


Fig. 23.  $h$ -convergence; (a) *composed* approach, (b) *hybrid* approach.

The second spatially dependent benchmark showed that the direct approach is unsuitable for solving such problems since it diverges within the first load increment. It has been proven that boundary condition stabilisation is crucial for the non-oscillatory solution and the convergence of the Newton–Raphson iteration method. *Composed* and *hybrid* approaches were successfully verified and proven capable of solving such problems. The *hybrid* approach was found to work successfully also with smaller  $\alpha_D$ s compared to the previous findings obtained on the elasto-plastic cases [51], where material parameters were not continuously differentiable. Compared to the previous study [51], where the *composed* approach suffered from the oscillatory solution and slow convergence, here it outperforms the *hybrid* approach, for which it was previously shown that it is only stable and robust enough to tackle discontinuously differentiable elasto-plasticity. In terms of time stepping, the convergence rate has proven to be of the 1st order, and the number of NRIs is increasing with increasing time step. The BCs stabilisation has proven not to significantly impact the  $h$ -convergence where the rate is still close to the one governed by the augmentation order. Overall, the *composed* approach proved to be most suitable method for solving such problems. Compared to FEM, it gives practically the same solutions.

In the future, the most promising *composed* approach will be used for modelling industrial processes where the visco-plastic laws characterises the material.

#### CRedit authorship contribution statement

**Gašper Vuga:** Writing – original draft, Visualization, Validation, Software, Resources, Methodology, Investigation, Formal analysis, Data curation, Conceptualization. **Boštjan Mavrič:** Writing – review & editing, Software, Resources, Methodology, Conceptualization. **Božidar Šarler:** Writing – review & editing, Supervision, Resources, Project administration, Methodology, Funding acquisition, Conceptualization.

#### Declaration of competing interest

The authors have no conflicts of interest to declare that are relevant to the content of this paper.

#### Data availability

Data will be made available on request.

#### Acknowledgements

This research was funded by the Slovenian Grant Agency by grant numbers P2-0162, L2-3173, and Z2-2640. The first author was supported by the Young Researcher’s grant.

#### Appendix A. Transforming the uniaxial case test with strain rate response problem to the system of ordinary differential equations

We observe Fig. 3 with the loading case I. Using the boundary conditions, the displacement field can be written as a linear function of position and time

$$u_x = C_x x t, \quad u_y = \hat{v} y t, \quad (\text{A.1})$$

where  $C_x$  is an unknown constant. Using Hooke’s law (3) and the strain decomposition (4) the relationship between stresses and strains can be written using the Voigt notation as

$$\begin{pmatrix} \sigma_{xx} \\ \sigma_{yy} \\ \sigma_{zz} \\ \sigma_{xy} \end{pmatrix} = \begin{pmatrix} (\lambda + 2G) & \lambda & \lambda & 0 \\ \lambda & (\lambda + 2G) & \lambda & 0 \\ \lambda & \lambda & (\lambda + 2G) & 0 \\ 0 & 0 & 0 & 2G \end{pmatrix} \begin{pmatrix} \epsilon_{xx} - \epsilon_{xx}^p \\ \epsilon_{yy} - \epsilon_{yy}^p \\ \epsilon_{zz} - \epsilon_{zz}^p \\ \epsilon_{xy} - \epsilon_{xy}^p \end{pmatrix}, \quad (\text{A.2})$$

where next to the plane strain assumption ( $\epsilon_{zz} = 0$ , but  $\epsilon_{zz}^p \neq 0$ ) all non-diagonal tensor elements are zero. Additionally, from traction boundary conditions it follows that  $\sigma_{xx} = 0$ . From here the expression is simplified as

$$\begin{pmatrix} 0 \\ \sigma_{yy} \\ \sigma_{zz} \end{pmatrix} = \begin{pmatrix} (\lambda + 2G) & \lambda & \lambda \\ \lambda & (\lambda + 2G) & \lambda \\ \lambda & \lambda & (\lambda + 2G) \end{pmatrix} \begin{pmatrix} \epsilon_{xx} - \epsilon_{xx}^p \\ \epsilon_{yy} - \epsilon_{yy}^p \\ -\epsilon_{zz}^p \end{pmatrix}, \quad (\text{A.3})$$

and evaluating total strains  $\{\epsilon_{xx}, \epsilon_{yy}\}$  from (A.1) it follows

$$\begin{pmatrix} 0 \\ \sigma_{yy} \\ \sigma_{zz} \end{pmatrix} = \begin{pmatrix} (\lambda + 2G) & \lambda & \lambda \\ \lambda & (\lambda + 2G) & \lambda \\ \lambda & \lambda & (\lambda + 2G) \end{pmatrix} \begin{pmatrix} C_x t - \epsilon_{xx}^p \\ \hat{v} t - \epsilon_{yy}^p \\ -\epsilon_{zz}^p \end{pmatrix}. \quad (\text{A.4})$$

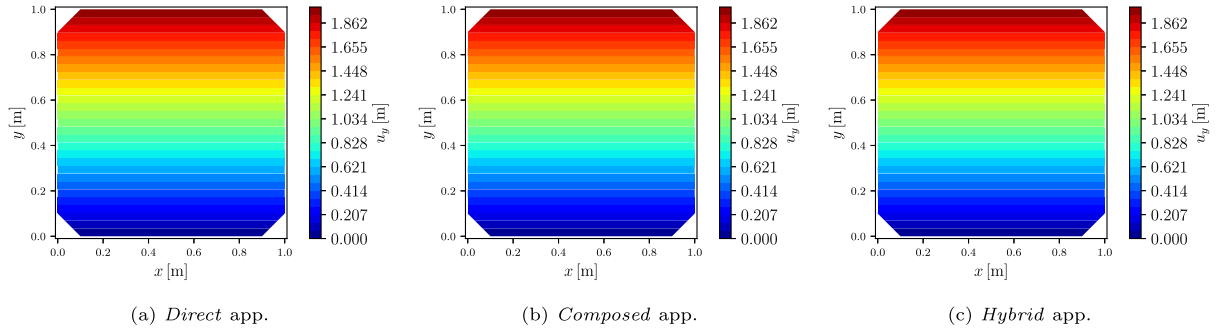


Fig. B.24. Displacement component  $u_y(p, t = t_{end})$ ; (a) direct approach, (b) composed approach, (c) hybrid approach.

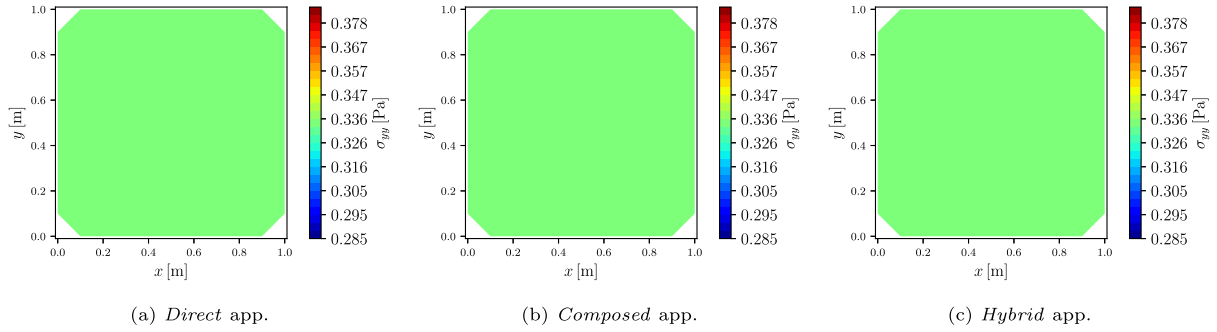


Fig. B.25. Stress component  $\sigma_{yy}(p, t = t_{end})$ ; (a) direct approach, (b) composed approach, (c) hybrid approach.

From the first equation, the constant  $C_x$  can be evaluated in terms of unknown plastic strain  $C_x = C_x(\epsilon^p)$ . This relation and the other two equations give the stress relations as  $\sigma_{yy} = \sigma_{yy}(\epsilon^p)$  and  $\sigma_{zz} = \sigma_{zz}(\epsilon^p)$ , from where it follows that  $s = s(\epsilon^p)$ . Moving to the visco-plastic flow rule (5) with the use of the Norton-Hoff law (6) we can write

$$\dot{\epsilon}^p = \left( \frac{\sigma_{vm}}{\mu} \right)^\beta N, \quad (\text{A.5})$$

where from the definition for the von Mises stress and the flow vector, we can write  $\sigma_{vm} = \sigma_{vm}(s(\epsilon^p))$ , and  $N = N(s(\epsilon^p))$ . From here, it follows that

$$\dot{\epsilon}^p = \left( \frac{\sigma_{vm}(\epsilon^p)}{\mu} \right)^\beta N(\epsilon^p), \quad (\text{A.6})$$

or shortly

$$\dot{\epsilon}^p = f(\epsilon^p) \quad (\text{A.7})$$

where  $f$  is a general non-linear function. Since all diagonal elements of  $\epsilon^p$  are non-zero, the relation (A.6) represents a system of three first-order non-linear ordinary differential equations that must be solved for  $\epsilon^p(t)$  where the initial condition is  $\epsilon^p(t = 0) = 0$ . With the solution, the constant  $C_x$  can be determined and from there the total and elastic strains, and stress from (A.4).

## Appendix B. Uniaxial case test with strain rate response solution

In this section, we provide additional results of the uniaxial case test (patch test) with strain rate loading (I. case with  $\dot{v} = 0.2$  m/s). In Fig. B.24 the displacement component  $u_y$  is shown over the whole domain obtained at the end of the simulation  $t_{end}$ . A linear solution, obtained the same with all of the presented approaches, can be seen.

In Fig. B.25 the stress component  $\sigma_{yy} = 0.335$  Pa is shown at the same time. As expected, the same constant solution is obtained for all three approaches. The calculated displacement and stress fields show a successful patch test result.

## References

- [1] Smith GD. Numerical solution of partial differential equations: Finite difference methods. 3rd ed. New York: Clarendon Press, Oxford Oxfordshire; 1986.
- [2] de Souza Neto EA, Peric D, Owen DR. Computational methods for plasticity: Theory and applications. Chichester, West Sussex, UK: John Wiley & Sons; 2011.
- [3] Cardiff P, Demirdžić I. Thirty years of the finite volume method for solid mechanics. Arch Comput Methods Eng 2021;28(5):3721–80. <http://dx.doi.org/10.1007/s11831-020-09523-0>.
- [4] Katsikadelis JT. The boundary element method for engineers and scientists: Theory and applications. Oxford, UK: Elsevier, Academic Press; 2016.
- [5] Atluri S. The meshless method (MLPG) method for domain BIE discretizations. Duluth, Minnesota, USA: Tech Science Press; 2004.
- [6] Liu GR. Meshfree methods: Moving beyond the finite element method. 2nd ed. Baton Rouge, Louisiana, USA: Taylor & Francis Group; 2009.
- [7] Liu GR, Gu YT. An introduction to meshfree methods and their programming. Dordrecht, Netherlands: Springer Dordrecht; 2005. <http://dx.doi.org/10.1007/1-4020-3468-7>.
- [8] Šarler B, Atluri SN. Recent studies in meshless and other novel computational methods. Duluth, Minnesota, USA: Tech Science Press; 2010.
- [9] Pepper D, Kassab A, Divo E. Introduction to finite element, boundary element, and meshless methods: with applications to heat transfer and fluid flow. New York, USA: ASME Press; 2014. <http://dx.doi.org/10.1115/1.860335>.
- [10] Rana K, Mavrič B, Zahoor R, Sarler B. A meshless solution of the compressible viscous flow in axisymmetric tubes with varying cross-sections. Eng Anal Bound Elem 2022;143:340–52. <http://dx.doi.org/10.1016/j.enganabound.2022.06.029>.
- [11] Slak J, Kosec G. On generation of node distributions for meshless PDE discretizations. SIAM J Sci Comput 2019;41(5):A3202–29. <http://dx.doi.org/10.1137/18M1231456>.
- [12] Jančič M, Kosec G. Strong form mesh-free hp-adaptive solution of linear elasticity problem. Eng Comput 2023;1–21. <http://dx.doi.org/10.1007/s00366-023-01843-6>.
- [13] Kovačević I, Sarler B. Solution of a phase-field model for dissolution of primary particles in binary aluminum alloys by an r-adaptive mesh-free method. Mater Sci Eng A 2005;413:423–8. <http://dx.doi.org/10.1016/j.msea.2005.09.034>.
- [14] Kargamov M, Ekhteraei Toussi H, Fariborz S. Elasto-plastic element-free Galerkin method. Comput Mech 2004;33(3):206–14. <http://dx.doi.org/10.1007/s00466-003-0521-5>.
- [15] Ji-fa Z, Wen-pu Z, Zheng Y. Meshfree method and its applications to elasto-plastic problems. J Zhejiang Univ Sci A Appl Phys Eng 2005;6(2):148–54. <http://dx.doi.org/10.1007/BF02847979>.

- [16] Mirzaei D, Hasanpour K. Direct meshless local Petrov–Galerkin method for elastodynamic analysis. *Acta Mech* 2016;227(3):619–32. <http://dx.doi.org/10.1007/s00707-015-1494-0>.
- [17] Cai L, Wang X, Wei J, Yao M. Meshless method modeling for crack initiation and propagation of continuous casting billets. *Metall Mater Trans B* 2021;52(5):3302–14. <http://dx.doi.org/10.1007/s11663-021-02257-9>.
- [18] Vaghefi R, Hematiyan MR, Nayebi A, Khosravifard A. A parametric study of the MLPG method for thermo-mechanical solidification analysis. *Eng Anal Bound Elem* 2018;89:10–24. <http://dx.doi.org/10.1016/j.enganabound.2018.01.006>, URL <https://www.sciencedirect.com/science/article/pii/S0955799717304745>.
- [19] Zhang X, Song KZ, Lu MW, Liu X. Meshless methods based on collocation with radial basis functions. *Comput Mech* 2000;26(4):333–43. <http://dx.doi.org/10.1007/s004660000181>.
- [20] Tolstykh A, Shirobokov D. On using radial basis functions in a finite difference mode with applications to elasticity problems. *Comput Mech* 2003;33(1):68–79. <http://dx.doi.org/10.1007/s00466-003-0501-9>.
- [21] Šarler B, Vertnik R. Meshfree explicit local radial basis function collocation method for diffusion problems. *Comput Math Appl* 2006;51(8):1269–82. <http://dx.doi.org/10.1016/j.camwa.2006.04.013>.
- [22] Flyer N, Fornberg B, Bayona V, Barnett GA. On the role of polynomials in RBF-FD approximations: I. interpolation and accuracy. *J Comput Phys* 2016;321(1):21–38. <http://dx.doi.org/10.1016/j.jcp.2016.05.026>.
- [23] Vertnik R, Šarler B. Local collocation approach for solving turbulent combined forced and natural convection problems. *Adv Appl Math Mech* 2011;3:259–79. <http://dx.doi.org/10.4208/aamm.10-10s2-01>.
- [24] Mramor K, Vertnik R, Šarler B. Meshless approach to the large-eddy simulation of the continuous casting process. *Eng Anal Bound Elem* 2022;138:319–38. <http://dx.doi.org/10.1016/j.enganabound.2022.03.001>.
- [25] Mramor K, Vertnik R, Sarler B. Development of three-dimensional LES based meshless model of continuous casting of steel. *Metals* 2022;12:1750. <http://dx.doi.org/10.3390/met12101750>.
- [26] Mramor K, Vertnik R, Šarler B. Simulation of continuous casting of steel under the influence of magnetic field using the local-radial basis-function collocation method. *Mater Tehnol* 2014;48:281–8.
- [27] Mramor K, Vertnik R, Šarler B. Application of the local RBF collocation method to natural convection in a 3D cavity influenced by a magnetic field. *Eng Anal Bound Elem* 2020;116(17–18):1–13. <http://dx.doi.org/10.1016/j.enganabound.2020.03.025>.
- [28] Dobravec T, Mavrič B, Šarler B. Reduction of discretisation-induced anisotropy in the phase-field modelling of dendritic growth by meshless approach. *Comput Mater Sci* 2020;172(1):109166. <http://dx.doi.org/10.1016/j.commatsci.2019.109166>.
- [29] Dobravec T, Mavrič B, Šarler B. Acceleration of RBF-FD meshless phase-field modelling of dendritic solidification by space-time adaptive approach. *Comput Math Appl* 2022;126:77–99. <http://dx.doi.org/10.1016/j.camwa.2022.09.008>, URL <https://www.sciencedirect.com/science/article/pii/S0898122122003881>.
- [30] Dobravec T, Mavrič B, Zahoor R, Šarler B. A coupled domain-boundary type meshless method for phase-field modelling of dendritic solidification with the fluid flow. *Internat J Numer Methods Heat Fluid Flow* 2023;33(8):2963–81. <http://dx.doi.org/10.1108/HFF-03-2023-0131>, Publisher: Emerald Publishing Limited.
- [31] Kovačević I, Sarler B. Solid-solid phase transformations in aluminium alloys described by a multiphase-field model. *Mater Sci Forum - MATER SCI FORUM* 2006;508:579–84. <http://dx.doi.org/10.4028/www.scientific.net/MSF.508.579>.
- [32] Bayona V, Sanchez-Sanz M, Fernández-Tarrazo E, Kindelan M. Micro-combustion modelling with RBF-FD: A high-order meshfree method for reactive flows in complex geometries. *Appl Math Model* 2021;94(2–3):635–55. <http://dx.doi.org/10.1016/j.apm.2021.01.032>.
- [33] Thakoor N, Tangman Y, Bhuruth M. RBF-FD schemes for option valuation under models with price-dependent and stochastic volatility. *Eng Anal Bound Elem* 2017;92. <http://dx.doi.org/10.1016/j.enganabound.2017.11.003>.
- [34] Hatič V, Mavrič B, Sarler B. Meshless simulation of a lid-driven cavity problem with a non-Newtonian fluid. *Eng Anal Bound Elem* 2021;131:86–99. <http://dx.doi.org/10.1016/j.enganabound.2021.06.015>.
- [35] Beggs K, Divó E, Kassab A. A meshless multiscale method for simulating hemodynamics. *Eng Anal Bound Elem* 2023;150:167–79. <http://dx.doi.org/10.1016/j.enganabound.2023.01.032>.
- [36] Asadi-Mehregan F, Assari P, Dehghan M. Numerical simulation of spatio-temporal spread of an infectious disease utilizing a collocation method based on local radial basis functions. *Eng Comput* 2024. <http://dx.doi.org/10.1007/s00366-023-01924-6>.
- [37] Liu Q, Hanoglu U, Rek Z, Šarler B. Simulation of temperature field in steel billets during reheating in pusher-type furnace by meshless method. *Math Comput Appl* 2024;29(3):30. <http://dx.doi.org/10.3390/mca29030030>, URL <https://www.mdpi.com/2297-8747/29/3/30>. Number: 3 Publisher: Multidisciplinary Digital Publishing Institute.
- [38] Stevens D, Power H, Cliffe K. A solution to linear elasticity using locally supported RBF collocation in a generalised finite-difference mode. *Eng Anal Bound Elem* 2013;37(1):32–41. <http://dx.doi.org/10.1016/j.enganabound.2012.08.005>.
- [39] Gerace S, Divó E, Kassab A. A localized radial-basis-function meshless method approach to axisymmetric thermo-elasticity. San Francisco, California, USA; 2006. <http://dx.doi.org/10.2514/6.2006-3788>.
- [40] Mavrič B, Sarler B. Local radial basis function collocation method for linear thermoelasticity in two dimensions. *Internat J Numer Methods Heat Fluid Flow* 2015;25:1488–510. <http://dx.doi.org/10.1108/HFF-11-2014-0359>.
- [41] Mavrič B, Šarler B. Application of the RBF collocation method to transient coupled thermoelasticity. *Internat J Numer Methods Heat Fluid Flow* 2017;27. <http://dx.doi.org/10.1108/HFF-03-2016-0110>.
- [42] Mavrič B. Meshless modeling of thermo-mechanics of low-frequency electromagnetic direct chill casting (Ph.D. thesis), Nova Gorica, Slovenia: University of Nova Gorica; 2017.
- [43] Hanoglu U, Islam S-U-I, Šarler B. Thermo-mechanical analysis of hot shape rolling of steel by a meshless method. *Procedia Eng* 2011;10:3181–6. <http://dx.doi.org/10.1016/j.proeng.2011.04.524>.
- [44] Hanoglu U, Šarler B. Simulation of hot shape rolling of steel in continuous rolling mill by local radial basis function collocation method. *CMES Comput Model Eng Sci* 2015;109–110(5):447–79. <http://dx.doi.org/10.3970/cmcs.2015.109.447>.
- [45] Hanoglu U, Šarler B. Multi-pass hot-rolling simulation using a meshless method. *Comput Struct* 2018;194:1–14. <http://dx.doi.org/10.1016/j.compstruc.2017.08.012>.
- [46] Hanoglu U, Šarler B. Hot rolling simulation system for steel based on advanced meshless solution. *Metals* 2019;9(7):788. <http://dx.doi.org/10.3390/met907788>.
- [47] Hanoglu U, Šarler B. Influence of casting defects on damage evolution and potential failures in hot rolling simulation system. *La Met Italiana Int J Italian Assoc Metall* 2023;02(114):48–52.
- [48] Cacciani N, Larsson E, Lauro A, Meggiolaro M, Scatto A, Tominec I, Villard P-F. A first meshless approach to simulation of the elastic behaviour of the diaphragm. In: Sherwin SJ, Moxey D, Peiró J, Vincent PE, Schwab C, editors. Spectral and high order methods for partial differential equations. ICOSAHOM 2018, Lecture notes in computational science and engineering, Cham, Switzerland: Springer International Publishing; 2020, p. 501–12. [http://dx.doi.org/10.1007/978-3-030-39647-3\\_40](http://dx.doi.org/10.1007/978-3-030-39647-3_40).
- [49] Strniša F, Jančič M, Kosec G. A meshless solution of a small-strain plasticity problem. In: 2022 45th jubilee international convention on information, communication and electronic technology. MIPRO, Opatija, Croatia; 2022, p. 257–62. <http://dx.doi.org/10.23919/MIPRO55190.2022.9803585>.
- [50] Mavrič B, Dobravec T, Vertnik R, Šarler B. A meshless thermomechanical travelling-slice model of continuous casting of steel. In: IOP conference series: materials science and engineering. Vol. 861, Jönköping, Sweden; 2020. <http://dx.doi.org/10.1088/1757-899X/861/1/012018>, 012018.
- [51] Vuga G, Mavrič B, Šarler B. An improved local radial basis function method for solving small-strain elasto-plasticity. *Comput Methods Appl Mech Engrg* 2024;418:116501. <http://dx.doi.org/10.1016/j.cma.2023.116501>.
- [52] Vuga G, Mavrič B, Šarler B. A hybrid radial basis function-finite difference method for modelling two-dimensional thermo-elasto-plasticity, part 1: Method formulation and testing. *Eng Anal Bound Elem* 2024;159:58–67. <http://dx.doi.org/10.1016/j.enganabound.2023.11.014>.
- [53] Vuga G, Mavrič B, Hanoglu U, Šarler B. A hybrid radial basis function - finite difference method for modelling two-dimensional thermo-elasto-plasticity, part 2: Application to cooling of hot-rolled steel bars on a cooling bed. *Eng Anal Bound Elem* 2024;159:331–41. <http://dx.doi.org/10.1016/j.enganabound.2023.12.001>.
- [54] Norton FH. The creep of steel at high temperatures. New York, USA: McGraw-Hill Book Company, Incorporated; 1929.
- [55] Kozłowski PF, Thomas BG, Azzi JA, Wang H. Simple constitutive equations for steel at high temperature. *Metall Trans A* 1992;23(3):903–18. <http://dx.doi.org/10.1007/BF02675567>.
- [56] Huespe A, Cardona A, Nigro N, Fachinotti V. Visco-plastic constitutive models of steel at high temperature. *J Mater Process Technol* 2000;102(1–3):143–52. [http://dx.doi.org/10.1016/S0924-0136\(00\)00442-8](http://dx.doi.org/10.1016/S0924-0136(00)00442-8), URL <https://linkinghub.elsevier.com/retrieve/pii/S0924013600004428>.
- [57] Vakhrushev A, Kharicha A, Wu M, Ludwig A, Nitzl G, Tang Y, Hackl G, Watzinger J, Rodrigues CMG. Norton–hoff model for deformation of growing solid shell of thin slab casting in funnel-shape mold. *J Iron Steel Res Int* 2022;29(1):88–102. <http://dx.doi.org/10.1007/s42243-021-00734-8>.
- [58] Ottosen NS, Ristinmaa M. The mechanics of constitutive modeling. London, UK: Elsevier; 2005.
- [59] Steinmann P, Runesson K. The catalogue of computational material models: Basic geometrically linear models in 1D. New York, USA: Springer; 2021. <http://dx.doi.org/10.1007/978-3-030-63684-5>.
- [60] Mavrič B, Šarler B. A collocation meshless method for linear thermoelasticity in 2D. In: 3rd international conference on computational methods for thermal problems. *thermaComp* 2014, Bled, Slovenia; 2014, p. 279–82.

- [61] Harris M, Kassab A, Divo E. Application of an RBF blending interpolation method to problems with shocks. *Comput Assist Methods Eng Sci* 2015;22(3):229–41.
- [62] Mathematica. 2019.
- [63] Trefethen LN, Bau III D. *Numerical linear algebra*. Philadelphia, Pennsylvania, USA: SIAM: Society for Industrial and Applied Mathematic; 1997.
- [64] Kassner ME. *Fundamentals of creep in metals and alloys*. 3rd ed.. Amsterdam: Elsevier; 2015.
- [65] DEFORM 2D. 2024, URL <http://www.deform.com>. [Accessed 24 April 2024].